Secondary twin variant selection in four types of double twins in titanium

Shun Xu, Mingyu Gong, Yanyao Jiang, Christophe Schuman, Jean-Sébastien Lecomte, Jian Wang

Secondary Twin Variant Selection in Four Types of Double Twins in Titanium

Shun Xu [a], Mingyu Gong [a], Yanyao Jiang [b], Christophe Schuman [c,d], Jean-Sébastien Lecomte [c,d], Jian Wang [a,*]

[a] Mechanical and Materials Engineering, University of Nebraska-Lincoln, Lincoln, NE, 68588, USA

[b] Department of Mechanical Engineering, University of Nevada, Reno; Reno, NV, 89557, USA

[c] Laboratoire d'Etude des Microstructures et de Mécanique des Matériaux (LEM3), CNRS UMR 7239,Université de Lorraine, F-57045 Metz, France

[d] Laboratory of Excellence on Design of Alloy Metals for low-mAss Structures (DAMAS), Université de Lorraine, France

Abstract

We experimentally characterized four types of double twins in pure titanium and discussed the selection of secondary twin variants based upon several different analyses. The four types of double twins are classified into two families according to their zone axes: co-family double twins and non-family double twins. Co-family double twins include $\{11\bar{2}2\}\rightarrow\{11\bar{2}1\}$ ($C_i^I \rightarrow T_j^{II}$) and $\{11\bar{2}1\} \rightarrow \{11\bar{2}4\}$ ($T_i^{II} \rightarrow C_j^{II}$) where both the primary twin and the secondary twin share the zone axis <10$\bar{1}$0>. Non-family double twins include $\{11\bar{2}2\}\rightarrow\{10\bar{1}2\}$ ($C_i^I \rightarrow T_j^I$) and $\{11\bar{2}4\} \rightarrow \{10\bar{1}2\}$ ($C_i^{II} \rightarrow T_j^I$) that have different zone axes with one along <11$\bar{2}$0> and the other along <10$\bar{1}$0>. Experimental observations reveal that one secondary twin variant ($C_i^I \rightarrow T_i^{II}$ for $\{11\bar{2}2\}\rightarrow\{11\bar{2}1\}$ double twins and $T_i^{II} \rightarrow C_i^{II}$ for $\{11\bar{2}1\} \rightarrow \{11\bar{2}4\}$ double twins) is prevailed over others in the co-family double twins and two secondary twin variants ($C_i^I \rightarrow T_i^I$ or T_{i+1}^I for $\{11\bar{2}2\}\rightarrow\{10\bar{1}2\}$ double twins and $C_i^{II} \rightarrow T_i^I$ or T_{i+1}^I for $\{11\bar{2}4\} \rightarrow \{10\bar{1}2\}$ double twins) are preferred in the non-family double twins. Secondary twin variant selection is analyzed based on the apparent Schmid factor (a-SF), the displacement gradient accommodation (DGA), the modified DGA (m-DGA), and the nucleation via dislocation dissociation (NDD). a-SFs associated with secondary twins are always positive once the primary twin is activated and the analysis based on a-SFs predicts no obvious preference for the selection of secondary twin variants. The m-DGA and NDD can correctly predict the selection of secondary twin variant in double twins, implying that the preferred secondary twin variant would, to the greatest extent, relax plastic deformation associated with the primary twinning and the nucleation of the secondary twin variant is facilitated by the accumulation of available gliding dislocations at the primary twin boundary.

Keywords: Titanium; Double Twin; Secondary Twin; Variant Selection

* **Corresponding author:** Jian Wang (jianwang@unl.edu)

1. Introduction

α-Titanium (Ti) is attractive in aerospace engineering, chemical industry, and medical implants due to light weight, high strength, excellent corrosion resistance, and good biocompatibility [1]. Research work has been focused on an understanding of the mechanisms and mechanics of plastic deformation associated with dislocation slips and twins in hexagonal close packed (HCP) crystals in the context of temperature and strain rate [2, 3], cyclic loading [4-8], strain path change [9-11], texture [12, 13], grain size [14, 15], and sample size [16]. At room temperature, the main slip systems in Ti include <***a***> slips on basal {0002}, prismatic $\{1\bar{1}00\}$, and pyramidal $\{1\bar{1}01\}$ plane [17, 18]. Dislocations associated with these <***a***> slips, however, cannot accommodate deformation along the *c*-axis. <***c***+***a***> slips on the $\{10\bar{1}1\}$ planes and twinning are possible shear mechanisms accommodating deformation in the *c*-axis direction. The dislocations associated with <***c***+***a***> slips have a large Burgers vector often with a non-planar core, making their activation energetically unfavourable. Twinning, on the other hand, takes place by the combined effect of non-lattice Burgers vector glide and atomic shuffling, and its activation results in the formation of a sheared domain where the crystal experiences a large reorientation with respect to the parent matrix.

Twinning competes favourably with <***c***+***a***> slips at low temperature or at high deformation rate when dislocations are difficult to overcome the threshold barriers. Tension twinning introduces a tensile strain and compression twinning generates a compressive strain along the *c*-axis of the crystal. $\{10\bar{1}2\}<\bar{1}011>$ tension twinning and $\{11\bar{2}2\}<11\overline{23}>$ compression twinning are commonly observed in α-titanium at room temperature [19-21] and are referred to as T_i^I and C_i^I, respectively, where the subscript represents variants from 1 to 6. Other twinning modes, $\{11\bar{2}1\}<\overline{11}26>$ tension twinning [22-25] and $\{11\bar{2}4\}<22\overline{43}>$ compression twining [26-28], can occur depending on temperature and the loading condition, and are referred to as T_i^{II} and C_i^{II}, respectively. For example, $\{11\bar{2}1\}$ and $\{11\bar{2}4\}$ twins are often observed in coarse-grained α-titanium at a high strain rate [26, 28-30]. Unlike dislocation slips, twinning causes the reorientation of the twinned domain and generates a localized shear strain along the twinning direction. Once a twin forms, another twin could be activated inside the twin. According to the sequence in nucleating twin variants, deformation twins can be classified into primary twin, secondary twin, and tertiary twin [31, 32].

Twin nucleation must precede twin propagation. Twin nucleation is driven by the local stress state and the local atomistic configurations while twin propagation is driven by long-

range stress state across the grain. Several criteria have been proposed to address the selection of twin variants observed in experiments [10, 30, 33-37] and to determine twin variants in polycrystalline plastic models [9, 10, 38-40]. The standard Schmid factor criterion (referred to as SF, i.e., the highest resolved shear stress selection rule) is extensively applied to account for variant selection of primary twins with the assumption that the local stress is identical to the nominal stress in polycrystalline aggregates [41]. Without considering specific nucleation sites and mechanisms, the SF offers a simple argument that a twin variant with the highest resolved shear stress is favourably activated. However, the local stresses inside a grain indeed differ from the externally applied stress [34, 37, 42]. To consider the local stress influence on twin nucleation at the meso and micro scales, Beyerlein *et al.* [43] introduced stress fluctuation criterion that was inspirited from the atomistic simulations of dislocation and grain boundary (GB) interactions. The nucleation of primary twins is treated as a stochastic event in terms of the selection of twin mode and twin variant. Such a theoretical speculation is consistent with the experimental observations that some twins are nucleated at GBs with low or negative SFs [37, 44, 45]. The criterion provides a geometric measure of how well a twin system is oriented with respect to an externally applied stress.

Nucleation of primary twins to some extent does show a preferred selection of twin variants [46]. To explain such a preference observed in experiments, Jonas *et al*. [34] proposed a displacement gradient accommodation (DGA) criterion for the selection of a primary twin variant. To predict twin variant, the displacement gradients associated with the primary twin are transformed into the crystal reference frame in a neighboring grain. A twin variant is selected when basal slips in the neighbouring grain can accommodate the transformed deformation. Such a notion provides a measurement of plastic deformation compatibility across a GB. Later, Shi *et al*. [37] extended the original DGA operation to all possible slip/twinning reference frames in the neighbouring grains, and found that the accommodation could be also realized through twinning often being referred to as a pair of cross-boundary twins [20, 47-49]. Inspired by atomistic simulations [50-54], Beyerlein *et al.* [33] proposed a nucleation criterion for secondary twinning according to dislocation dissociation (NDD) without using the highest resolved shear stress concept and the plastic deformation compatibility. The criterion is based on an assumption that twin nucleation is facilitated by the accumulation, reaction, and dissociation of gliding dislocations at primary twin boundary [33].

The aforementioned three criteria have advantages and disadvantages. Efforts have been made to improve the criteria, such as apparent-SF (a-SF) and modified DGA [29, 37, 55]. Xu

et al. [29] modified the DGA criterion (referred to as m-DGA) to predict secondary twin variant with a focus on minimizing the resultant plastic deformation in the matrix associated with double twinning. In other words, a selected secondary twin variant should, to the greatest extent, diminish the shear deformation resulting from the primary twin [29]. On the other hand, there has been no systematic assessment of these existing criteria in terms of their capability to predict primary and secondary twinning. In this work, coarse-grained polycrystalline α-titanium was subjected to uniaxial compression at room temperature along the normal direction (ND) of the rolled sheet. We detected four twin modes, $\{11\bar{2}2\}$ and $\{11\bar{2}4\}$ compression twins and $\{10\bar{1}2\}$ and $\{11\bar{2}1\}$ tension twins. More interestingly, four types of double twins were observed. By comparing with the experimental observations, we systematically evaluate the existing criteria for their capabilities to predict secondary twin variant selection in the double twins. Advantages of each criterion are discussed based on the experimental and theoretical results.

2. Secondary twin variants in four types of double twins

2.1 Crystallographic characteristics of double twins

$\{10\bar{1}m\}$ (m=1, 2, 3) type and $\{11\bar{2}n\}$ (n=1, 2, 4) type twins are often observed in hexagonal metals, as depicted in Fig. 1a and Fig. 1b, respectively. The former type has the zone axis parallel to $<11\bar{2}0>$ and the latter type has the zone axis parallel to $<10\bar{1}0>$. Due to 12 rotational symmetry matrices in an HCP structure, there are six equivalent variants for each twinning system. Under mechanical deformation at room temperature, $\{10\bar{1}2\}$ tension twins and $\{11\bar{2}2\}$ compression twins are commonly observed in α-Titanium [20, 30, 56]. $\{11\bar{2}1\}$ tension twins and $\{11\bar{2}4\}$ compression twins can also be produced but have a low volume fraction. When primary twins form, the twinned domain may be twinned further, forming double twins. To facilitate discussions, T_i^I and T_i^{II} (i =1, 2, …6) are used to denote the six $\{10\bar{1}2\}$ and the six $\{11\bar{2}1\}$ tension twin variants, respectively, and C_i^I and C_i^{II} (i =1, 2, …6) represent respectively the six $\{11\bar{2}2\}$ and the six $\{11\bar{2}4\}$ compression twin variants. For example, T_1^I is the $(10\bar{1}2)[\bar{1}011]$ twin variant, T_1^{II} is the $(11\bar{2}1)[\bar{1}\bar{1}26]$ twin variant, C_1^I is the $(11\bar{2}2)[11\overline{23}]$ twin variant, and C_1^{II} is the $(11\bar{2}4\})[22\overline{43}]$ variant, as depicted in Fig. 1. According to the crystallography of an HCP structure, T_i^I twin variant can be obtained by rotating the T_1^I variant $(i\text{-}1)\times60$ degrees about the <0001> axis. The same operation is applicable to other twins.

Four types of double twins that were observed in deformed Ti specimens can be classified into two families: co-family and non-family double twins. The co-family double twins include $\{11\bar{2}2\}\rightarrow\{11\bar{2}1\}$ ($C_i^I \rightarrow T_j^{II}$) and $\{11\bar{2}1\} \rightarrow \{11\bar{2}4\}$ ($T_i^{II} \rightarrow C_j^{II}$) where both twins share the zone axis $<10\bar{1}0>$ and the arrow in the notation refers to the process from the primary twinning to the secondary twinning. The non-family double twins include $\{11\bar{2}2\}\rightarrow\{10\bar{1}2\}$ ($C_i^I \rightarrow T_j^I$) and $\{11\bar{2}4\} \rightarrow \{10\bar{1}2\}$ ($C_i^{II} \rightarrow T_j^I$) where both twins have different zone axes with one along $<11\bar{2}0>$ and the other along $<10\bar{1}0>$.

Each type of double twins can be further classified into a few groups according to the misorientation between the secondary twin variant and the parent grain. Taking $\{11\bar{2}2\}\rightarrow\{11\bar{2}1\}$ ($C_i^I \rightarrow T_j^{II}$) co-family double twins as an example, $\{11\bar{2}2\}\rightarrow\{11\bar{2}1\}$ double twins can be categorized into four groups according to the misorientation angle between a secondary twin variant $\{11\bar{2}1\}$ and the parent grain. Group I includes $C_i^I \rightarrow T_i^{II}$ double twins that hold a misorientation angle of 29.5° about the axis $<1\bar{1}00>$. Group II includes $C_i^I \rightarrow T_{i+1}^{II}$ and $C_i^I \rightarrow T_{i+5}^{II}$ double twins that have a misorientation angle of 55° about the axis $<\overline{10}\ 5\ 5\ \bar{3}>$. Group III includes $C_i^I \rightarrow T_{i+3}^{II}$ double twins that hold a misorientation angle of 80.6° around the axis $<1\bar{1}00>$. Group IV includes $C_i^I \rightarrow T_{i+2}^{II}$ and $C_i^I \rightarrow T_{i+4}^{II}$ double twins that hold a misorientation angle of 86.8° around the axis $<\overline{15}\ 10\ 5\ \bar{3}>$. Table 1 summaries the geometric characteristics of the six $\{11\bar{2}1\}$ secondary twin variants inside the $(11\bar{2}2)[11\overline{23}]$ (C_1^I) primary twin. For convenience in performing the NDD analysis, we also characterize the intersection lines between twin planes, slip planes and the primary twin boundary. The intersection line between a secondary twin plane and a primary twin plane is denoted by $\boldsymbol{l}_{(S\text{-}P)}$ and that between a basal plane and a primary twin plane is represented by $\boldsymbol{l}_{(B\text{-}P)}$. The angle between $\boldsymbol{l}_{(S\text{-}P)}$ and $\boldsymbol{l}_{(B\text{-}P)}$ is denoted by $\theta_{(SB/P)}$. Similarly, $\{11\bar{2}1\}\rightarrow\{11\bar{2}4\}$ double twins are divided into four groups (refer to Table 1). Group I and Group III have one variant while Group II and Group IV have two variants. Unlike co-family double twins, $\{11\bar{2}2\}\rightarrow\{10\bar{1}2\}$ and $\{11\bar{2}4\}\rightarrow\{10\bar{1}2\}$ non-family double twins are divided into three groups (Table 1) with each group containing two twin variants.

Table 1. Geometric characteristics of the primary twin and secondary twins.

Secondary twin	misorientation	Group	Nomination	$\boldsymbol{l}_{(S\text{-}P)}$	$\boldsymbol{l}_{(B\text{-}P)}$	$\theta_{(SB/P)}$
$(11\bar{2}2)[11\bar{2}\bar{3}]$ (C_i^I) →{$11\bar{2}1$} double twins						
$(11\bar{2}1)[\bar{1}\bar{1}26]$	**<$1\bar{1}00$> 29.5°**	**I**	$\boldsymbol{C_i^I \rightarrow T_i^{II}}$	**$[1\bar{1}00]$**	**$[1\bar{1}00]$**	**0°**
$(\bar{1}2\bar{1}1)[1\bar{2}16]$	<$\bar{1}0$ 5 5 $\bar{3}$> 55°	II	$C_i^I \rightarrow T_{i+1}^{II}$	$[\bar{1}\bar{1}23]$	$[1\bar{1}00]$	**90°**
$(\bar{2}111)[2\bar{1}\bar{1}6]$	<$\bar{1}5$ 10 5 $\bar{3}$> 86.8°	IV	$C_i^I \rightarrow T_{i+2}^{II}$	$[1\bar{3}23]$	$[1\bar{1}00]$	58.4°
$(\bar{1}\bar{1}21)[11\bar{2}6]$	<$1\bar{1}00$> 80.6°	III	$C_i^I \rightarrow T_{i+3}^{II}$	$[1\bar{1}00]$	$[1\bar{1}00]$	0°
$(1\bar{2}11)[\bar{1}2\bar{1}6]$	<$\bar{1}5$ 10 5 $\bar{3}$> 86.8°	IV	$C_i^I \rightarrow T_{i+4}^{II}$	$[\bar{3}123]$	$[1\bar{1}00]$	58.4°
$(2\bar{1}\bar{1}1)[\bar{2}116]$	<$\bar{1}0$ 5 5 $\bar{3}$> 55°	II	$C_i^I \rightarrow T_{i+5}^{II}$	$[\bar{1}\bar{1}23]$	$[1\bar{1}00]$	90°
$(11\bar{2}1)[\bar{1}\bar{1}26]$ (T_i^{II}) →{$11\bar{2}4$} double twins						
$(11\bar{2}4)[22\bar{4}\bar{3}]$	**<$1\bar{1}00$> 68.2°**	**III**	$\boldsymbol{T_i^{II} \rightarrow C_i^{II}}$	**$[1\bar{1}00]$**	**$[1\bar{1}00]$**	**0°**
$(\bar{1}2\bar{1}4)[\bar{2}4\bar{2}3]$	<$\bar{3}5$ 10 25 9> 88.3°	IV	$T_i^{II} \rightarrow C_{i+1}^{II}$	$[3\bar{4}13]$	$[1\bar{1}00]$	39.5°
$(\bar{2}114)[\bar{4}22\bar{3}]$	<6 $\bar{1}0$ 4 3> 65.6°	II	$T_i^{II} \rightarrow C_{i+2}^{II}$	$[4\bar{5}13]$	$[1\bar{1}00]$	32.6°
$(\bar{1}\bar{1}24)[\bar{2}\bar{2}4\bar{3}]$	<$1\bar{1}00$> 41.9°	I	$T_i^{II} \rightarrow C_{i+3}^{II}$	$[1\bar{1}00]$	$[1\bar{1}00]$	0°
$(1\bar{2}14)[2\bar{4}2\bar{3}]$	<6 $\bar{1}0$ 4 3> 65.6°	II	$T_i^{II} \rightarrow C_{i+4}^{II}$	$[5\bar{4}\bar{1}3]$	$[1\bar{1}00]$	32.6°
$(2\bar{1}\bar{1}4)[4\bar{2}\bar{2}3]$	<$\bar{3}5$ 10 25 9> 88.3°	IV	$T_i^{II} \rightarrow C_{i+5}^{II}$	$[4\bar{3}\bar{1}3]$	$[1\bar{1}00]$	39.5°
$(11\bar{2}2)[11\bar{2}\bar{3}]$ (C_i^I) →{$10\bar{1}2$} double twins						
$(10\bar{1}2)[\bar{1}011]$	**<$\bar{5}503$> 48.4°**	**II**	$\boldsymbol{C_i^I \rightarrow T_i^I}$	**$[\bar{4}223]$**	**$[1\bar{1}00]$**	**47.3°**
$(01\bar{1}2)[0\bar{1}11]$	**<$\bar{5}503$> 48.4°**	**II**	$\boldsymbol{C_i^I \rightarrow T_{i+1}^I}$	**$[2\bar{4}23]$**	**$[1\bar{1}00]$**	**47.3°**
$(\bar{1}102)[1\bar{1}01]$	<$7\bar{4}\bar{3}0$> 87.9°	III	$C_i^I \rightarrow T_{i+2}^I$	$[2\bar{4}23]$	$[1\bar{1}00]$	47.3°
$(\bar{1}012)[10\bar{1}1]$	<$5\bar{1}\bar{4}3$> 41.3°	I	$C_i^I \rightarrow T_{i+3}^I$	$[\bar{1}0\ 8\ 2\ 3]$	$[1\bar{1}00]$	19.8°
$(0\bar{1}12)[01\bar{1}1]$	<$5\bar{1}\bar{4}3$> 41.3°	I	$C_i^I \rightarrow T_{i+4}^I$	$[8\ \bar{1}0\ 2\ 3]$	$[1\bar{1}00]$	19.8°
$(1\bar{1}02)[\bar{1}101]$	<$7\bar{4}\bar{3}0$> 87.9°	III	$C_i^I \rightarrow T_{i+5}^I$	$[\bar{4}223]$	$[1\bar{1}00]$	47.3°
$(11\bar{2}4)[22\bar{4}\bar{3}]$ (C_i^{II}) → {$10\bar{1}2$} double twins						
$(10\bar{1}2)[\bar{1}011]$	**<$11\bar{2}\bar{3}$> 39.5°**	**I**	$\boldsymbol{C_i^{II} \rightarrow T_i^I}$	**$[22\bar{4}\bar{3}]$**	**$[1\bar{1}00]$**	**90°**
$(01\bar{1}2)[0\bar{1}11]$	**<$11\bar{2}\bar{3}$> 39.5°**	**I**	$\boldsymbol{C_i^{II} \rightarrow T_{i+1}^I}$	**$[\bar{2}\bar{2}43]$**	**$[1\bar{1}00]$**	**90°**
$(\bar{1}102)[1\bar{1}01]$	<7 20 $\bar{2}7$ $\bar{2}0$> 44.3°	II	$C_i^{II} \rightarrow T_{i+2}^I$	$[1\bar{5}43]$	$[1\bar{1}00]$	55.8°
$(\bar{1}012)[10\bar{1}1]$	<$\bar{1}3$ $\bar{2}6$ 39 4> 89.5°	III	$C_i^{II} \rightarrow T_{i+3}^I$	$[10\ \bar{1}4\ 4\ 3]$	$[1\bar{1}00]$	20.2°
$(0\bar{1}12)[01\bar{1}1]$	<$\bar{1}3$ $\bar{2}6$ 39 4> 89.5°	III	$C_i^{II} \rightarrow T_{i+4}^I$	$[\bar{1}4\ 10\ 4\ 3]$	$[1\bar{1}00]$	20.2°
$(1\bar{1}02)[\bar{1}101]$	<7 20 $\bar{2}7$ $\bar{2}0$> 44.3°	II	$C_i^{II} \rightarrow T_{i+5}^I$	$[\bar{5}143]$	$[1\bar{1}00]$	55.8°

2.2 Experimental observations

A commercial rolled pure titanium T40 sheet (ASTM grade 2) with a thickness of 1.5 mm was annealed in a vacuum furnace at 800 ^{o}C for 2 hours. The annealed sheet was subjected to a compressive strain of 8.7% at a strain rate 1.0E-3 s^{-1} at room temperature using a Zwick 120T machine. The compression direction was parallel to the normal direction (ND) of the rolled sheet. The surface of the deformed sample was ground with SiC papers of grits from 1200$^{\#}$ to 4000$^{\#}$. Electrolytic polishing was performed using a solution of 10% perchloric acid and 90% methanol at 35 V for five seconds at 5 ^{o} and electron backscatter diffraction (EBSD) measurements were made in a JEOL JSM-6500F field emission gun scanning electron microscopy (SEM) equipped with an EBSD camera and the AZtec acquisition software package (Oxford Instruments).

In Ti, $\{11\bar{2}1\}$ tension twinning rotates the crystal by ~35° around a $<1\bar{1}00>$ axis. $\{10\bar{1}2\}$ tension twinning results in a rotation of the crystal by ~87° around a $<1\bar{2}10>$ axis. $\{11\bar{2}2\}$ compression twinning rotates the twinned domain by ~64° around a $<1\bar{1}00>$ axis. $\{11\bar{2}4\}$ compression twinning rotates the twinned domain by ~77° around a $<1\bar{1}00>$ axis. According to these crystallographic characteristics, we further characterized four types of double twins in deformed specimens.

Fig. 2a shows an EBSD pattern where a $\{11\bar{2}2\}$ compression twin contains secondary $\{11\bar{2}1\}$ and $\{10\bar{1}2\}$ tension twins. The boundaries formed by the $\{11\bar{2}1\}$ tension twin, $\{10\bar{1}2\}$ tension twin, and $\{11\bar{2}2\}$ compression twin with the parent crystal are indicated in Fig.2b in yellow, red, and green, respectively, with a tolerance of ±5° deviation from the ideal crystallographic axis and angle. Such a tolerance is used for the other double twin observations made throughout the current work. With the help of pole figures in Fig. 2c, the misorientation angle between $(\bar{2}112)$ planes in the primary twin and in the matrix is 0.89°, which is the smallest among all possibilities. The dashed black line in Fig. 2c indicates the trace of the twinning plane, which is in agreement with the detected trace of the twinning plane shown in Fig. 2b. Therefore, C_3^I twin variant is identified as the primary twin. In the pole figure of $\{11\bar{2}1\}$ planes (Fig. 2d), the misorientation angle between $(\bar{2}111)$ planes in the C_3^I primary twin and the secondary twin is 3.12°. The trace of this twinning plane in Fig. 2d is practically parallel to that in Fig. 2b. T_3^{II} is, therefore, identified as a secondary twin variant. The double twin configuration can be regarded as $C_3^I \rightarrow T_3^{II}$, which belongs to Group I as indicated in Table 1. In the EBSD results, 43 $\{11\bar{2}2\}\rightarrow\{11\bar{2}1\}$ double twins are detected including 41 Group I and

two Group II double twins. Therefore, Group I, i.e., $C_i^I \rightarrow T_i^{II}$ is the prevailed double twin over the others.

Fig. 3a shows an EBSD pattern where the $\{11\bar{2}1\}$ tension twin contains secondary $\{11\bar{2}4\}$ compression twins and the twin boundaries are indicated in Fig. 3b. With the help of pole figures in Fig. 3c, the misorientation angle between $(\bar{1}2\bar{1}1)$ planes in the primary twin and that in the matrix is 1.46°, which is the closest among all possibilities. In addition, the dashed black line in Fig. 3c indicates the trace of the twinning plane, which is in agreement with the detected trace of the twinning plane as shown in Fig. 3a. Therefore, T_2^{II} twin variant is identified as the primary twin. In the pole figure of $\{11\bar{2}4\}$ planes (Fig. 3d), the misorientation angle between $(\bar{1}2\bar{1}4)$ planes in the T_2^{II} primary twin and the secondary twin is 2.37°. The trace of this twinning plane in Fig. 3d is almost parallel to that in Fig. 3b. C_2^{II} is thus the secondary twin variant. The double twin configuration can be described as $T_2^{II} \rightarrow C_2^{II}$, which belongs to Group III as indicated in Table 1. It is noted that such kind of double twins are rarely observed in our experiments. More experiments are required for a solid conclusion.

Fig. 4a shows an EBSD pattern where the $\{11\bar{2}2\}$ compression twin contains secondary $\{10\bar{1}2\}$ tension twins and the twin boundaries are indicated in Fig. 4b. From the pole figures shown in Fig. 4c, C_2^I twin variant can be identified as the primary twin. In the pole figure of $\{10\bar{1}2\}$ planes (Fig. 4d), T_2^I is the secondary twin variant. The double twin can be described as $C_2^I \rightarrow T_2^I$ which belongs to Group II. In the C_2^I primary twin, there are two variants T_2^I and T_3^I belonging to Group I. A similar analysis was applied to $\{11\bar{2}2\}\rightarrow\{10\bar{1}2\}$ double twins in Fig. 4e, and the results indicate a detection of $C_4^I \rightarrow T_5^I$ double twin (Group II). In the EBSD results, 425 $\{11\bar{2}4\}\rightarrow\{10\bar{1}2\}$ double twins were detected and 85.6% of them belong to Group II double twins. Therefore, the preferred double twins can be described as $C_i^I \rightarrow T_i^I$ or T_{i+1}^I. The a-SF analysis will be used to further identify the variant selection in the preferred group.

Fig. 5a shows an EBSD pattern where the $\{11\bar{2}4\}$ compression twin contains secondary $\{10\bar{1}2\}$ tension twins. The twin boundaries are indicated in Fig. 5b. The pole figures in Fig. 5c indicates that C_6^{II} twin variant is the primary twin. In the pole figure of $\{10\bar{1}2\}$ planes (Fig. 5d), T_6^I is the active secondary twin variant. The double twin configuration can be described as $C_6^{II} \rightarrow T_6^I$, which belongs to Group I. By applying a similar analysis was applied to $\{11\bar{2}4\}\rightarrow\{10\bar{1}2\}$ double twins in Fig. 5e, $C_4^{II} \rightarrow T_5^I$ double twin (Group I) can be detected. In the EBSD results, 41 $\{11\bar{2}4\}\rightarrow\{10\bar{1}2\}$ double twins were identified and all of them belong to

Group I double twins. Therefore, Group I double twin, $C_i^{II} \rightarrow T_i^I$ or T_{i+1}^I, is the prevailed double twins over other two groups.

In summary, co-family double twins can be categorized into four groups and only one double twin variant is prevailed in each primary twin. For $\{11\bar{2}2\}\rightarrow\{11\bar{2}1\}$ double twins, the dominant double twins are described as $C_i^I \rightarrow T_i^{II}$. For $\{11\bar{2}1\} \rightarrow \{11\bar{2}4\}$ double twins, the dominant double twins are described as $T_i^{II} \rightarrow C_i^{II}$. Non-family double twins can be divided into three groups, and two variants are possibly selected in the prevailed group. For $\{11\bar{2}2\}\rightarrow\{10\bar{1}2\}$ double twins, the preferred double twins can be described as $C_i^I \rightarrow T_i^I$ or T_{i+1}^I (Group II). For $\{11\bar{2}4\} \rightarrow \{10\bar{1}2\}$ double twins, the preferred double twins can be described as $C_i^{II} \rightarrow T_i^I$ or T_{i+1}^I (Group I).

3. Selection of secondary twin variants

The mode and variant of secondary twins are inevitably related to the local stresses. An analysis of the stress field could be simplified regarding the secondary twinning knowing that the resolved shear stress associated with primary twinning is positive. The resolved shear stress associated with a secondary twin can be directly related to the resolved shear stress activating the primary twinning. With this notion in mind, Xu *et al.* [29] recently proposed a concept of apparent SF (a-SF). First, a primary loading domain in which the active primary twin is the most favourable variant among all possibilities is identified in an inverse pole figure. The SFs associated with the six secondary twin variants are calculated under an applied loading condition in the primary loading domain, and the results are plotted in the primary loading domain. The prevailed secondary twin variant is corresponding to the variant with relative high SFs in most of the primary loading domain. By comparing the SFs with the experiments [21], Xu *et al.* found that a twin variant can be activated with a relatively large SF but not necessary at the highest SF value among all the variants.

Experimental observations reveal that a secondary twin variant associated with sequential twinning or transmission twinning [27, 48, 49, 57, 58] has a strong correlation with the incoming twin or slip [59-61], and a secondary twin variant associated with double twinning is related to the primary twin [10, 33, 62, 63]. The DGA and the m-DGA criteria have been applied to predict the selection of these secondary twin variants [29, 55, 64]. Here we will compare the predictions according to the DGA and m-DGA with experimental observations. Furthermore, we perform a nucleation analysis on the primary twin boundary based on the gliding dislocation dissociation (NDD). In what follows, we will examine these criteria for

selecting secondary twin variant in four types of double twins experimentally observed in Ti.

3.1 {11$\bar{2}$2}→{11$\bar{2}$1} co-family double twins

3.1a Apparent SF (a-SF) analysis

{11$\bar{2}$2} twin variant C_1^I is chosen as the primary twin for the analysis without losing generality. The primary loading domain is determined according to the SF associated with C_1^I twin when a grain is subjected to uniaxial compression. SFs of the six {11$\bar{2}$2} twin variants are determined for a given loading direction relative to the grain orientation. The loading directions with SFs being larger than 0.3 are grouped into the primary loading domain (associated with primary twin C_1^I) in an inverse pole figure (IPF) as shown in Fig. 6a. Afterward, the SFs associated with the six {11$\bar{2}$1} secondary twin variants T_j^{II} (j=1...6) inside the primary twin C_1^I are determined for a loading case in the primary loading domain and are plotted into IPFs (Fig. 6b-g) where the red color indicates positive SFs and the blue color denotes negative SFs. The results show that twin variants T_1^{II} and T_4^{II} hold high SFs under most loading directions, while other four secondary twin variants have moderate SFs only at specific loading cases and low SFs at most loading cases. Results in Fig. 6b-g suggest that activation of secondary twin variants T_1^{II} and T_4^{II} has a higher probability than the other four primary compression twin variants. When the SFs of the secondary twin variants larger than 0.2 are selected for an IPF, the area of the loading domain is virtually zero for T_2^{II}, T_3^{II}, T_5^{II}, and T_6^{II}, while the area for T_1^{II} and T_4^{II} are non-zero and identical. Therefore, an a-SF analysis seems to be able to explain the high probability for nucleating secondary twin variants in Group I and Group III, and the low frequency for Group II and Group IV twin variants. More importantly, the a-SF analysis clearly shows that the SFs for six twin variants are positive in most loading domain as long as the primary twin is subjected to a positive resolved shear stress.

3.1b Nucleation via dislocation dissociation (NDD)

Assuming that a secondary twin is nucleated via twinning dislocations from the primary twin boundary, we first analyze the geometric characteristics of the intersection between secondary twin planes and the primary twin plane, as shown in Fig. 7. The intersection line between secondary twin variants (belonging to Group I and Group III) and the primary twin plane is parallel to [1$\bar{1}$00], which also lies on the basal plane (Fig. 7a). Therefore, the emission of twinning dislocations can be considered as the dissociation of basal <***a***> dislocations on the secondary twin plane. For Group II, the intersection line between the primary twin plane and

secondary twin plane is parallel to $[\bar{1}\bar{1}23]$, which lies on prismatic plane $\{1\bar{1}00\}$ and is perpendicular to the intersection line between the basal and the primary twin plane (Fig. 7b). As a result, emitting twinning dislocations can be considered as the dissociation of prismatic <***a***> dislocation on the secondary twin plane. If <***c***+***a***> dislocations on the prismatic plane can be activated, emitting twinning can be also dissociated into emissary twin dislocations (TDs) on the secondary twin plane. For Group IV, the intersection line between the primary and secondary twin planes is along $<\bar{3}123>$ which does not lie on any usual slip planes (Fig. 7c). Therefore, dislocation dissociation mechanisms would be difficult to activate secondary twins unless dislocations can easily climb on the primary twin plane and are parallel to the intersection line along $<\bar{3}123>$.

Fig. 7d illustrates secondary twinning mechanisms associated with the dissociation of <***a***> dislocations into TDs. When $(0002)<11\bar{2}0>$ dislocations approach the primary twin boundary, Fig. 7e illustrates the dissociation of the dislocation into TDs associated with Group I (T_1^{II}) and Group III (T_4^{II}) secondary twins. For Groups I to III, an <***a***> dislocation, b_a, can be dissociated into x secondary twining dislocations $xb_t^{\{11\bar{2}1\}}$ and a residual dislocation b_r^m, where the subscript m represents the mth (m=1, 2, 4, 6) secondary twin,

$$b_i \Rightarrow b_r^m + xb_t^{\{11\bar{2}1\}} \tag{1}$$

In Eq.(1) $b_i = a_i$ with a magnitude of 0.295 nm for α-Ti. The three base vectors a_1, a_2, and a_3 are equal to $\frac{1}{3}[2\bar{1}\bar{1}0]$, $\frac{1}{3}[\bar{1}2\bar{1}0]$, $\frac{1}{3}[\bar{1}\bar{1}20]$, respectively. The Burgers vector of $\{11\bar{2}1\}$ TD $b_t^{\{11\bar{2}1\}}$ $= \lambda<\bar{1}\bar{1}26>$, $\lambda=\frac{1}{3+12k^2} = 0.0301$ for Ti (a=0.295 nm and c=0.4683 nm, k=c/a). For T_1^{II} and T_4^{II} secondary twins, three <***a***> dislocations on basal plane can act as sources for the dissociation. However, there is only one $\boldsymbol{b}_3$ dislocation on prismatic plane that acts as the source for the dissociation into secondary twin dislocations belonging to T_2^{II} and T_6^{II} secondary twins. According to Frank's law, the change in the elastic energy associated with these dissociations is described as follows for T_1^{II}:

$$|b_3|^2 = \left|b_r^1\right|^2 + \left|xb_t^{(11\bar{2}1)}\right|^2 \tag{2}$$

When x=1, the elastic energy before and after the dissociation is identical. Results summarized in Table 2 reveal that the dissociation of <***a***> dislocations only favorably produces twinning dislocation associated with T_1^{II} secondary twin variant. The other dissociations corresponding

to T_2^{II}, T_4^{II} and T_6^{II} secondary twins are accompanied with an increase in the elastic energy after dissociation. It is noted that only the dissociation of $\boldsymbol{b}_3$ dislocation is energetically favorable for producing twinning dislocation of T_1^{II} secondary twin variant. In other words, $C_i^I \rightarrow T_i^{II}$ is predominant among all double twinning. Such a speculation is consistent with the a-SF analysis and agrees with experimental observation.

Table 2. Nucleation of $\{11\bar{2}1\}$ secondary twin variants in the $(11\bar{2}2)[11\bar{2}\bar{3}]$ primary twin.

NDD Analysis

Secondary twin	b_t	b_i	b_r^m	$\lvert b_i\rvert^2$	x	$\lvert xb_t\rvert^2$	$\lvert b_r^m\rvert^2$
		b_1	$[0.70\ \overline{0.3}\ \overline{0.4}\ \overline{0.18}]$	8.70	1	0.78	10.27
$(11\bar{2}1)[\overline{11}26]\ T_1^{II}$	**$\lambda[\overline{11}26]$**	b_2	$[\overline{0.3}\ 0.70\ \overline{0.4}\ \overline{0.18}]$	8.70	1	0.78	10.27
		b_3	**$-0.3[1\ 1\ \bar{2}\ 0.6]$**	**8.70**	**1**	**0.78**	**7.92**
$(\bar{1}2\bar{1}1)[1\bar{2}16]\ T_2^{II}$	$\lambda[1\bar{2}16]$	b_3	$-0.09[4\ 3\ \bar{7}\ 2]$	8.70	1	0.78	8.70
		b_1	$-0.09[\bar{7}\ 4\ 3\ 2]$	8.70	1	0.78	8.70
$(\overline{11}21)[11\bar{2}6]\ T_4^{II}$	$\lambda[11\bar{2}6]$	b_2	$-0.09[4\ \bar{7}\ 3\ 2]$	8.70	1	0.78	8.70
		b_3	$-0.18[2\ 2\ \bar{4}\ 1]$	8.70	1	0.78	11.06
$(2\overline{11}1)[\bar{2}116]\ T_6^{II}$	$\lambda[\bar{2}116]$	b_3	$-0.09[3\ 4\ \bar{7}\ 2]$	8.70	1	0.78	8.70

DGA and m-DGA Analysis

Secondary twin	Group	D_{ST} in the crystal reference frame of the parent grain	D_{ST} in the twinning reference frame of the primary twin
$(11\bar{2}1)[\overline{11}26]\ T_1^{II}$	**I**	$\begin{bmatrix} 0.0655 & 0.0378 & 0.0809 \\ 0.0378 & 0.0218 & 0.0467 \\ -0.0707 & -0.0408 & -0.0873 \end{bmatrix}$	$\begin{bmatrix} -0.1549 & 0 & -0.5893 \\ 0 & 0 & 0 \\ 0.0407 & 0 & 0.1549 \end{bmatrix}$
$(\bar{1}2\bar{1}1)[1\bar{2}16]\ T_2^{II}$	II	$\begin{bmatrix} 0.0808 & -0.0466 & 0.0294 \\ 0.0901 & -0.052 & 0.0328 \\ -0.0791 & 0.0457 & -0.0288 \end{bmatrix}$	$\begin{bmatrix} 0 & -0.4614 & -0.3150 \\ 0 & -0.1354 & -0.0924 \\ 0 & 0.1984 & 0.1354 \end{bmatrix}$
$(\bar{2}111)[2\overline{11}6]\ T_3^{II}$	IV	$\begin{bmatrix} 0.0551 & -0.0802 & -0.0685 \\ 0.0565 & -0.0822 & -0.0674 \\ -0.0227 & 0.033 & 0.0271 \end{bmatrix}$	$\begin{bmatrix} 0.2328 & -0.3783 & 0.1115 \\ 0.0833 & -0.1354 & 0.0399 \\ -0.2035 & 0.3307 & -0.0974 \end{bmatrix}$
$(\overline{11}21)[11\bar{2}6]\ T_4^{II}$	III	$\begin{bmatrix} -0.0183 & -0.0106 & -0.1485 \\ -0.0106 & -0.0061 & -0.0858 \\ 0.003 & 0.0017 & 0.0244 \end{bmatrix}$	$\begin{bmatrix} 0.3108 & 0 & 0.2636 \\ 0 & 0 & 0 \\ -0.3664 & 0 & -0.3108 \end{bmatrix}$
$(1\bar{2}11)[\bar{1}2\bar{1}6]\ T_5^{II}$	IV	$\begin{bmatrix} -0.0581 & 0.1219 & -0.0912 \\ -0.0148 & 0.0311 & -0.0232 \\ 0.0173 & -0.0362 & 0.0271 \end{bmatrix}$	$\begin{bmatrix} 0.2328 & 0.3783 & 0.1115 \\ -0.0833 & -0.1354 & -0.0399 \\ -0.2035 & -0.3307 & -0.0974 \end{bmatrix}$
$(2\overline{11}1)[\bar{2}116]\ T_6^{II}$	II	$\begin{bmatrix} 0 & 0.1367 & 0.0431 \\ 0 & 0.0288 & 0.0091 \\ 0 & -0.0914 & -0.0288 \end{bmatrix}$	$\begin{bmatrix} 0 & 0.4616 & -0.3150 \\ 0 & -0.1354 & 0.0924 \\ 0 & -0.1984 & 0.1354 \end{bmatrix}$

3.1c Displacement gradient accommodation analysis (DGA and m-DGA)

The original DGA criterion predicts a preference of nucleation of a twin variant whose deformation can be accommodated by easy slips in the vicinity of the twin domain. For a $(11\bar{2}2)[11\bar{2}\bar{3}]$ primary twin (C_1^I), the displacement gradients induced by six possible secondary $\{11\bar{2}1\}$ twin (D_{ST}) variants in its twinning frame can be resolved into three directions, $x'\|[10\bar{1}0]$, $y'\|[\bar{1}2\bar{1}0]$, and $z'\|[0001]$, in the crystal frame of the parent grain. $e_{x'z'}$ and $e_{y'z'}$ represent the accommodation by double and single basal slips, respectively; $e_{z'x'}$ and $e_{z'y'}$ indicate the accommodation by twinning, and $e_{x'y'}$ and $e_{y'x'}$ are associated with the accommodation by double and single prismatic slips, respectively [34]. The transformed displacement gradient tensors, D_{ST} for the six potential secondary twin variants are listed in the first column in Table. 2, where the accommodation associated with basal slip, prismatic slip and twinning is indicated in red, blue and green font, respectively. The accommodation components required in the parent grain are defined as [d_1, d_2, d_3], where $d_1=|e_{x'z'}|+|e_{y'z'}|$, $d_2=|e_{x'y'}|+|e_{y'x'}|$, and $d_3=|e_{z'x'}|+|e_{z'y'}|$ represent the accommodation in the parent grain through basal slip, prismatic slip, and twinning, respectively. It can be seen that the induced deformation gradient by the secondary twins belonging to Group I can be easily accommodated by basal slip and twinning with accommodation components of [**0.1276**, 0.0756, **0.1115**]. For Group II, the accommodation is realized through prismatic slip and twinning corresponding to [0.0622, **0.1367**, **0.1248**] for $(\bar{1}2\bar{1}1)[1\bar{2}16]$ and [0.0522, **0.1367**, **0.0914**] for $(2\bar{1}\bar{1}1)[\bar{2}116]$). For Group III, basal slip is the main accommodation system according to [**0.2343**, 0.0212, 0.0043]. For Group IV, much accommodation is required through basal and prismatic slip according to [**0.1359**, **0.1367**, 0.0557] for $(\bar{2}111)[2\bar{1}\bar{1}6]$ and [**0.1144**, **0.1367**, 0.0535] for $(1\bar{2}11)[\bar{1}2\bar{1}6]$). Therefore, the original DGA cannot distinguish the prevailed secondary twin variant over other variants.

When the DGA criterion is modifed to focus on minimizing the resultant plastic deformation associated with the double twinning (m-DGA), the displacement gradient created by the six potential secondary twin variants is transformed into the twinning reference frame of the primary twin. The results are listed in Table. 2. The e_{13} component (light blue) indicates the ability of a secondary twin variant to diminish the strain created by the primary twin. A larger magnitude of the e_{13} component will more effectively diminish the resultant strain. It can be seen that Group I can maximally diminish the strain induced by the $(11\bar{2}2)[11\bar{2}\bar{3}]$ primary twin. In addition, Group II double twins can also partially decrease the strain associated with the primary twin while Group I is not effective. The m-DGA predicts a clear

order in terms of activating the secondary twin variants, Group I ($C_i^I \rightarrow T_i^{II}$) > Group II ($C_i^I \rightarrow T_{i+1}^{II}, C_i^I \rightarrow T_{i+5}^{II}$) > Group IV ($C_i^I \rightarrow T_{i+2}^{II}, C_i^I \rightarrow T_{i+4}^{II}$) > Group III ($C_i^I \rightarrow T_{i+3}^{II}$). Such predictions are consistent with the a-SF and NDD analysis, more importantly, agree with the experimental observation.

3.2 {11$\bar{2}$1}→{11$\bar{2}$4} double twins

3.2a Apparent SF (a-SF) analysis

Fig. 8 shows IPFs of the primary loading domain associated with the primary twin T_1^{II}. The SFs of the six {11$\bar{2}$4} twin variants C_j^{II} (j=1...6) inside the primary twin T_1^{II} are plotted in Fig. 8b-g. We integrated the area of the domains where the SFs are larger than 0.2. The ratios of the domain areas for four Groups are 1.79:2.27:1:1.66. The average SFs for four Groups are 0.40 for Group I, 0.38 for Group II, 0.34 for Group III, and 0.36 for Group IV. Secondary twin variants in Group II are predicted to be activated with a slightly higher possibility. However, experimental observations do not support such a prediction.

3.2b Nucleation via dislocation dissociation (NDD)

Fig. 9 shows the geometric characteristics of four groups of {11$\bar{2}$1}→{11$\bar{2}$4} double twins. The intersection line between the primary twin plane and the secondary twin variants belonging to Group III and Group I is parallel to [1$\bar{1}$00], which is parallel to the intersection line between the basal plane and the primary twin plane, as depicted in Fig. 9a. Correspondingly, basal <***a***> dislocation can be dissociated to produce Group I and Group III secondary twins. For Group II, the common axis between the primary and secondary twin plane aligns parallel to <4$\bar{5}$13>, which lies in pyramidal {$\bar{1}$011} planes and has an angle of 32.6° with the intersection line between the primary twin plane and the basal plane. Dissociation of dislocations on {$\bar{1}$011} pyramidal planes is required to activate Group II secondary twins, which is relatively difficult. For Group IV, the common lines between the primary and secondary twin planes are along <3$\bar{4}$13>, which do not lie on any usual slip planes, and have an angle of 39.5° with the intersection line between the primary twin plane and the basal plane. As a result, dislocation dissociation is difficult unless dislocations can easily climb on the primary twin plane. Nucleation based on dissociation of basal <***a***> dislocation is more likely for the secondary twin variants belonging to Group I and Group III. When a (0002)<11$\bar{2}$0> dislocation approaches the primary twin boundary, it can be dissociated into x twinning dislocations $xb_t^{\{11\bar{2}4\}}$ associated with Group III (C_1^{II}) and Group I (C_4^{II}) secondary twins and residual dislocations b_r^m, where the subscript m represents the mth (m=1, 4) secondary twin.

$$b_i \Rightarrow b_r^{\mathrm{m}} + x b_t^{\{11\bar{2}4\}} \quad (3)$$

Table 3 summarizes the dissociation of a basal <***a***> dislocation into secondary twins belonging to Groups I, II, and III. For C_1^{II} (Group III), a (0002)<11$\bar{2}$0> dislocation, a b_3 can be dissociated into three secondary twining dislocations $3b_t^{(11\bar{2}4)}$ (x=3), and a residual dislocation b_r^{m} (m=1). The dissociation process is energetically favorable according to Frank's law $\left(|b_3|^2 > \left|b_r^1\right|^2 + \left|3b_t^{(11\bar{2}4)}\right|^2\right)$. When a b_1 or b_2 dislocation acts as the source for dissociation, the production of only one C_1^{II} secondary twining dislocation $b_t^{(11\bar{2}4)}$ (x=1) is energetically favored as listed in Table 3. However, for C_4^{II} (Group III), a (0002)<11$\bar{2}$0> dislocation, b_i dissociates into one secondary twining dislocation $b_t^{(\bar{1}\bar{1}24)}$ (x=1) and a residual one b_r^{m} (m=4). This dissociation process is energetically unfavourable due to the increase in the line energy $\left(|b_i|^2 < \left|b_r^4\right|^2 + \left|b_t^{(\bar{1}\bar{1}24)}\right|^2\right)$. The magnitude of Burgers vector of {11$\bar{2}$4} twinning dislocation is equal to $\frac{c^2-2a^2}{\sqrt{4a^2+c^2}}$, 0.6 nm for α-Ti. According to the theory, the energetically favorable dissociation is associated with the formation of secondary twin variant C_1^{II} (Group III), and the other twin variants are difficult to be activated according to dislocation dissociation. The NDD prediction agrees with the experimental observations.

3.2c Displacement gradient accommodation analysis (DGA and m-DGA)

For a DGA analysis, the displacement gradients induced by six possible secondary {11$\bar{2}$2} twins (D_{ST}) in (11$\bar{2}$1)[$\bar{1}$126] primary twin (T_1^{II}) can be expressed in the crystal frame of the parent grain as listed in the first column of Table 3. Much accommodation for Group III is made through twinning according to the accommodation components [0.0195, 0.0414, **0.2196**]. For Groups I and II, the accommodation is mainly realised by basal slip according to the accommodation components [**0.2382**, 0.0092, 0.0009] for Group I and [**0.1684**, 0.0869, 0.0402] for Group II ($\bar{2}$114)[$\bar{4}$22$\bar{3}$] and [**0.1685**, 0.0957, 0.0331] for Group II (1$\bar{2}$14)[2$\bar{4}$2$\bar{3}$]. For Group IV, the accommodation is conducted through twinning according to the accommodation components [0.0741, 0.0992, **0.1275**] for ($\bar{1}$2$\bar{1}$4)[$\bar{2}$4$\bar{2}\bar{3}$] and [0.0762, 0.0868, **0.1488**] for (2$\bar{1}\bar{1}$4)[4$\bar{2}\bar{2}\bar{3}$]. The results suggest that Group I and II are prevailed over Groups III and IV because plastic relaxation via twinning is more difficult than that via twinning. Such a prediction is different from that based on the NDD and the experimental results.

According the m-DGA analysis, we transformed the displacement gradient induced by six potential secondary twins into the twinning reference frame of the primary twin. The results listed in the second column in Table 3 indicate that Group III can, to a great extent, accommodate the strain induced by the $(11\bar{2}1)[\bar{1}\bar{1}26]$ primary twin. Group IV secondary twins can also partially accommodate the strain associated with the primary twin. Other secondary twins do not reduce the resultant deformation produced by the double twins. The prediction according to the m-DGA is consistent with that based on the NDD analysis and experimental observations.

Table 3. Nucleation of $\{11\bar{2}4\}$ secondary twin variants in the $(11\bar{2}1)[\bar{1}\bar{1}26]$ primary twin.

NDD Analysis							
Secondary twin	b_t	b_i	b_r^m	$\|b_i\|^2$	x	$\|xb_t\|^2$	$\|b_r^m\|^2$
		b_1	[0.61 $\overline{0.39}$ $\overline{0.22}$ 0.08]	8.70	1	0.36	7.68
$(11\bar{2}4)[22\bar{4}\bar{3}]$ C_1^{II}	**$\lambda[22\bar{4}\bar{3}]$**	b_2	[$\overline{0.39}$ 0.61 $\overline{0.22}$ 0.08]	8.70	1	0.36	7.68
		b_3	**[0.17 0.17 $\overline{0.34}$ 0.24]**	**8.70**	**3**	**3.24**	**3.62**
		b_1	[0.72 $\overline{0.28}$ $\overline{0.44}$ 0.08]	8.70	1	0.36	10.45
$(\bar{1}\bar{1}24)[\bar{2}\bar{2}43]$ C_4^{II}	$\lambda[\bar{2}\bar{2}43]$	b_2	[$\overline{0.28}$ 0.72 $\overline{0.44}$ 0.08]	8.70	1	0.36	10.45
		b_3	[0.39 0.39 $\overline{0.78}$ 0.08]	8.70	1	0.36	11.84

DGA and m-DGA Analysis			
Secondary twin	Group	D_{ST} in the crystal reference frame of the parent grain	D_{ST} in the twinning reference frame of the primary twin
$(11\bar{2}4)[22\bar{4}\bar{3}]$ C_1^{II}	**III**	$\begin{bmatrix} 0.0359 & 0.0207 & -0.0124 \\ 0.0207 & 0.012 & -0.0071 \\ 0.1392 & 0.0804 & -0.0479 \end{bmatrix}$	$\begin{bmatrix} -0.1021 & 0 & -0.1509 \\ 0 & 0 & 0 \\ -0.0691 & 0 & 0.1021 \end{bmatrix}$
$(\bar{1}2\bar{1}4)[\bar{2}4\bar{2}\bar{3}]$ C_2^{II}	IV	$\begin{bmatrix} 0.0474 & -0.0062 & -0.025 \\ -0.093 & 0.0121 & 0.0491 \\ 0.1128 & -0.0147 & -0.0596 \end{bmatrix}$	$\begin{bmatrix} -0.1022 & 0.0842 & -0.0831 \\ -0.0976 & 0.0803 & -0.0794 \\ 0.0269 & -0.0221 & 0.0219 \end{bmatrix}$
$(\bar{2}114)[\bar{4}22\bar{3}]$ C_3^{II}	II	$\begin{bmatrix} -0.0189 & 0.016 & 0.0355 \\ -0.0709 & 0.0598 & 0.1329 \\ 0.0218 & -0.0184 & -0.0409 \end{bmatrix}$	$\begin{bmatrix} -0.0879 & 0.0563 & 0.0064 \\ -0.1254 & 0.0803 & 0.0091 \\ -0.1036 & 0.0664 & 0.0075 \end{bmatrix}$
$(\bar{1}\bar{1}24)[\bar{2}\bar{2}43]$ C_4^{II}	I	$\begin{bmatrix} 0.0079 & 0.0046 & 0.151 \\ 0.0046 & 0.0026 & 0.0872 \\ -0.0006 & -0.0003 & -0.0106 \end{bmatrix}$	$\begin{bmatrix} -0.0735 & 0 & 0.0281 \\ 0 & 0 & 0 \\ -0.1919 & 0 & 0.0735 \end{bmatrix}$
$(1\bar{2}14)[2\bar{4}2\bar{3}]$ C_5^{II}	II	$\begin{bmatrix} 0.0164 & -0.0913 & 0.1328 \\ -0.0044 & 0.0245 & -0.0357 \\ -0.005 & 0.0281 & -0.0409 \end{bmatrix}$	$\begin{bmatrix} -0.0879 & -0.0563 & 0.0064 \\ 0.1254 & 0.0803 & -0.0091 \\ -0.1036 & -0.0664 & 0.0075 \end{bmatrix}$
$(2\bar{1}\bar{1}4)[4\bar{2}\bar{2}3]$ C_6^{II}	IV	$\begin{bmatrix} -0.022 & -0.0529 & 0.03 \\ 0.0339 & 0.0816 & -0.0462 \\ 0.0437 & 0.1051 & -0.0596 \end{bmatrix}$	$\begin{bmatrix} -0.1022 & -0.0842 & -0.0831 \\ 0.0976 & 0.0803 & 0.0794 \\ 0.0269 & 0.0221 & 0.0219 \end{bmatrix}$

3.3 $\{11\bar{2}2\}\rightarrow\{10\bar{1}2\}$ non-family double twins

3.3a Apparent SF (a-SF) analysis

Fig. 10a shows IPFs of the primary loading domain associated with the primary twin C_1^I. Under this primary loading, the SFs associated with six potential $\{10\bar{1}2\}$ twin variants T_j^I (j=1...6) are calculated inside the primary twin C_1^{II} and plotted in Fig. 10b-g. The results show that secondary twin variants (T_i^I and T_{i+3}^I) exhibit very similar SFs due to the approximate 90° angle between their twin planes. The SFs of T_3^I and T_6^I secondary twin variants are very low at most loading cases, while other four secondary twin variants hold high SFs. When the SFs of secondary twins larger than 0.2 are selected, the area of the loading domain is almost zero for T_3^I and T_6^I, while the area of this loading domain and the average SF in this loading area are almost identical for other four secondary twin variants. Therefore, a-SF analysis is unable to distinguish the four secondary twin variants.

3.3b Nucleation via dislocation dissociation (NDD)

As listed in Table 4, the intersection line between the primary twinning plane and the secondary twinning planes in Group II and Group III is along <$\bar{4}$223>, which lies in prismatic $\{10\bar{1}0\}$ plane and has an angle of 47.3° with the intersection between the primary twin plane and the basal plane. This provides a geometric favorite for the dissociation of prismatic <***a***> dislocation into the secondary twin dislocations belonging to the two groups. However, the intersection line between Group I secondary twinning plane and the primary twinning plane does not lie on any usual slip planes. The dissociation mechanism for nucleating secondary twins in Group I requires dislocation climb on the primary twin plane. A prismatic <***a***> dislocation can dissociate into *x* secondary $\{10\bar{1}2\}$ twinning dislocation $xb_t^{\{10\bar{1}2\}}$ and a residual dislocation b_r^m (m=1, 2, 3, 6).

$$b_i \Rightarrow b_r^m + xb_t^{\{10\bar{1}2\}} \tag{4}$$

As listed in Table 4, a b_1 or b_2 dislocation can dissociate into three secondary $\{10\bar{1}2\}$ twinning dislocations (*x*=3) associated with T_1^I and T_2^I variants (Group II), respectively, which is energetically favorable according to Frank's law. However, a b_2 or b_1 dislocation dissociates into only one secondary $\{10\bar{1}2\}$ twinning dislocation (*x*=1) associated with T_3^I and T_6^I variant (Group III), respectively, and the dissociation is energetically unfavorable due to the increase in the elastic energy after dissociation. Therefore, the dislocation dissociation analysis shows a preference of $\{11\bar{2}2\}\rightarrow\{10\bar{1}2\}$ double twins, i.e., the $C_i^I \rightarrow T_i^I$ or T_{i+1}^I double twins (Group II).

3.3c Displacement gradient accommodation analysis (DGA and m-DGA)

According to the DGA analysis, the displacement gradients induced by the six possible secondary $\{10\bar{1}2\}$ twins in $(11\bar{2}2)[11\bar{2}\bar{3}]$ primary twin (C_1^I) can be expressed in the crystal frame of the parent grain and are listed in the first column of Table 4 for a DGA analysis. It can be seen that for Group I, the displacement gradient induced by the secondary twin can be mainly accommodated through basal slip according to the accommodation components [**0.199**, 0.0789, 0.0304] for $(\bar{1}012)[10\bar{1}1]$ and [**0.1591**, 0.0871, 0.0342] for $(0\bar{1}12)[01\bar{1}1]$. For Group II, twinning is the main accommodation carrier according to the accommodation components [0.0229, 0.0789, **0.2091**] for $(10\bar{1}2)[\bar{1}011]$ and [0.0216, 0.085, **0.1715**] for $(01\bar{1}2)[0\bar{1}11]$. For Group III, the accommodation can be achieved through prismatic slip in the parent according to the accommodation components [0.0614, **0.1578**, 0.0596] for $(\bar{1}102)[1\bar{1}01]$ and [0.0685, **0.1578**, 0.0591] for $(1\bar{1}02)[\bar{1}101]$. According to the DGA analysis, Group III twins are the preferred secondary twins since prismatic slip is the easiest slip to activate in α-titanium. Such a prediction is inconsistent with the experimental observation and is different from that obtained from the NDD.

Displacement gradients created by the six potential double twins were transformed into the twinning reference frames of the primary twin for a m-DGA analysis. The results listed in the secondary column in Table 4 indicate that Group II can, to a great extent, accommodate the strain induced by the $(11\bar{2}2)[11\bar{2}\bar{3}]$ primary twin. In contrast, Group III double twins can accommodate little strain induced by the primary twin, and Group I cannot accommodate the strain. The m-DGA analysis is consistent with experimental observations and the prediction by the NDD.

Table 4. Nucleation of $\{10\bar{1}2\}$ secondary twin variants in the $(11\bar{2}2)[11\bar{2}\bar{3}]$ primary twin.

NDD Analysis							
Secondary twin	b_t	b_i	b_r^m	$\|b_i\|^2$	x	$\|xb_t\|^2$	$\|b_r^m\|^2$
$(10\bar{1}2)[\bar{1}011]$ T_1^I	**$\lambda[\bar{1}011]$**	**b_1**	**$[\overline{0.41}\ 0.33\ 0.08\ \overline{0.26}]$**	**8.70**	**3**	**3.24**	**5.16**
$(01\bar{1}2)[0\bar{1}11]$ T_2^I	**$\lambda[0\bar{1}11]$**	**b_2**	**$[0.33\ \overline{0.41}\ 0.08\ \overline{0.26}]$**	**8.70**	**3**	**3.24**	**5.16**
$(\bar{1}102)[1\bar{1}01]$ T_3^I	$\lambda[1\bar{1}01]$	b_2	$[0.42\ \overline{0.75}\ 0.33\ \overline{0.09}]$	8.70	1	0.36	11.34
$(1\bar{1}02)[\bar{1}101]$ T_6^I	$\lambda[\bar{1}101]$	b_1	$[\overline{0.75}\ 0.42\ 0.33\ \overline{0.09}]$	8.70	1	0.36	11.34

DGA and m-DGA Analysis			
Secondary twin	Group	D_{ST} in the crystal reference frame of the parent grain	D_{ST} in the twinning reference frame of the primary twin

$(10\bar{1}2)[\bar{1}011]$ T_1^I	**II**	$\begin{bmatrix} 0.0518 & 0.0622 & 0.0173 \\ -0.0167 & -0.02 & -0.0056 \\ -0.095 & -0.1141 & -0.0318 \end{bmatrix}$	$\begin{bmatrix} 0.0498 & 0.0539 & -0.1417 \\ -0.0201 & -0.0218 & 0.0573 \\ 0.0098 & 0.0106 & -0.0280 \end{bmatrix}$
$(01\bar{1}2)[0\bar{1}11]$ T_2^I	**II**	$\begin{bmatrix} 0.0177 & 0.003 & 0.0038 \\ 0.082 & 0.0141 & 0.0178 \\ -0.1463 & -0.0252 & -0.0318 \end{bmatrix}$	$\begin{bmatrix} 0.0498 & -0.0539 & -0.1417 \\ 0.0201 & -0.0218 & -0.0573 \\ 0.0098 & -0.0106 & -0.0280 \end{bmatrix}$
$(\bar{1}102)[1\bar{1}01]$ T_3^I	III	$\begin{bmatrix} 0.0255 & -0.007 & -0.0089 \\ 0.1508 & -0.0417 & -0.0525 \\ -0.0467 & 0.0129 & 0.0163 \end{bmatrix}$	$\begin{bmatrix} 0.0624 & -0.0676 & -0.0393 \\ 0.0805 & -0.0872 & -0.0507 \\ -0.0393 & 0.0426 & 0.0248 \end{bmatrix}$
$(\bar{1}012)[10\bar{1}1]$ T_4^I	I	$\begin{bmatrix} 0.0536 & -0.0088 & -0.0862 \\ 0.0701 & -0.0115 & -0.1128 \\ 0.0261 & -0.0043 & -0.0421 \end{bmatrix}$	$\begin{bmatrix} 0.0379 & -0.0137 & 0.0041 \\ 0.0604 & -0.0218 & 0.0066 \\ -0.1474 & 0.0532 & -0.0161 \end{bmatrix}$
$(0\bar{1}12)[01\bar{1}1]$ T_5^I	I	$\begin{bmatrix} 0.0313 & 0.083 & -0.1408 \\ 0.0041 & 0.0108 & -0.0183 \\ 0.0094 & 0.0248 & -0.0421 \end{bmatrix}$	$\begin{bmatrix} 0.0379 & 0.0137 & 0.0041 \\ -0.0604 & -0.0218 & -0.0066 \\ -0.1474 & -0.0532 & -0.0161 \end{bmatrix}$
$(1\bar{1}02)[\bar{1}101]$ T_6^I	III	$\begin{bmatrix} 0.0373 & 0.1439 & -0.0499 \\ -0.0139 & -0.0539 & 0.0186 \\ -0.0122 & -0.0469 & 0.0163 \end{bmatrix}$	$\begin{bmatrix} 0.0624 & 0.0676 & -0.0393 \\ -0.0805 & -0.0872 & 0.0507 \\ -0.0393 & -0.0426 & 0.0248 \end{bmatrix}$

3.4 $\{11\bar{2}4\}\rightarrow\{10\bar{1}2\}$ non-family double twins

3.4a Apparent SF (a-SF) analysis

Fig. 11 shows the primary loading domain associated with the primary twin C_1^{II} and six potential $\{10\bar{1}2\}$ twin variants T_j^I (j=1...6) into an IPF. Except for the difference in the primary loading domain from that in Fig. 10, the conclusion is the same as that in the case of $\{11\bar{2}2\}\rightarrow\{10\bar{1}2\}$ double twins. In other words, a-SF cannot distinguish the preference of secondary twin variants.

3.4b Nucleation via dislocation dissociation (NDD)

The crystallographic feature of three groups of $\{11\bar{2}4\}\rightarrow\{10\bar{1}2\}$ double twins is illustrated in Fig. 12 when $(11\bar{2}4)[22\bar{4}\bar{3}]$ (C_1^{II}) is the primary twin. The intersection line between two secondary twin variants belonging to Group I (T_1^I and T_2^I) is parallel to $[22\bar{4}\bar{3}]$, which lies in prismatic $(1\bar{1}00)$ plane and is perpendicular to the intersection line between the primary twin plane and basal plane as indicated in Fig. 12a. Thus, basal <***a***> dislocations cannot dissociate into twinning dislocations associated with the two secondary twins. Instead, <***a***> dislocation on the prismatic plane can dissociate to produce secondary twins. For T_3^I and T_6^I in Group II, the common axis between the primary and secondary twin plane aligns parallel to $[1\bar{5}43]$ and $[\bar{5}143]$, which lies on pyramidal planes $(10\bar{1}1)$ and $(01\bar{1}1)$ as indicated in Fig. 12b. However, dislocations on pyramidal planes are rarely activated. In addition, the angle between the common axis and the intersection line between the basal plane and the primary twin plane is 55.8°. The dissociation based on basal <***a***> dislocations requires the rotation of basal <***a***>

dislocation line for 55.8° via the climb on the twin plane. Thus, nucleating secondary twins in Group II lacks dislocation sources. For T_4^I and T_5^I in Group III, the common axis between the primary and secondary twin plane is parallel to [10 $\bar{1}$4 4 3] and [$\bar{1}$4 10 4 3] (refer to Fig. 12c), which do not lie on any usual slip planes. However, the angle between the common axis and the intersection line between the basal plane and the primary twin plane is 20.2°. Compared with Group II, there is a less dependence on dislocation climb. Regarding secondary twins T_1^I and T_2^I in Group I, there is only one <***a***> dislocation with the Burgers vector b_3 that can be dissociated into x secondary $\{10\bar{1}2\}$ twining dislocation $xb_t^{(10\bar{1}2)}$ and a residual one b_r^m (m=1, 2),

$$b_i \Rightarrow b_r^m + xb_t^{\{10\bar{1}2\}} \tag{5}$$

As listed in Table 5, b_3 is dissociated into three secondary twining dislocation $3b_t^{\{10\bar{1}2\}}$ (x=3). The dissociation is energetically favorable due to the decrease in the elastic energy after dissociation. Therefore, secondary twins in Group I should be prevailed over others, and secondary twins in Group III are likely activated than those in Group II.

3.4c Displacement gradient accommodation analysis (DGA and m-DGA)

For a DGA analysis, the displacement gradients induced by six possible secondary $\{10\bar{1}2\}$ twin in its twinning frame can be expressed in the crystal frame of the parent grain as listed in the first column of Table 5. For Group I, the main accommodation system is basal slip according to the accommodation components [**0.1241**, 0.095, 0.0757] for $(10\bar{1}2)[\bar{1}011]$ and [**0.1589**, 0.0852, 0.0554] for $(01\bar{1}2)[0\bar{1}11]$. For Group II, the accommodation can be mainly realized by prismatic slip according to the accommodation components [0.0342, **0.1705**, 0.0319] for $(\bar{1}102)[1\bar{1}01]$ and [0.0366, **0.1705**, 0.0329] for $(1\bar{1}02)[\bar{1}101]$. For Group III, the accommodation is carried out by twinning according to the accommodation components [0.0589, 0.0973, **0.1409**] for $(\bar{1}012)[10\bar{1}1]$ and [0.0487, 0.0852, **0.1744**] for $(0\bar{1}12)[01\bar{1}1]$. Accordingly, Group II variants should be prevailed among three groups because prismatic slip is the easiest slip to activate in α-titanium. Group III variants are unlikely activated because of the accommodation by twinning based on the DGA analysis.

According to the m-DGA analysis, the displacement gradient created by six potential double twins was transformed into the twinning reference frame of the primary twin, and the results are listed in the secondary column in Table 5. Group I can, to the greatest extent,

accommodate the strain induced by the $(11\bar{2}4)[22\bar{4}\bar{3}]$ primary twin. In contrast, Group II double twins can accommodate little strain induced by the primary twin while Group III cannot accommodate the strain. Therefore, the m-DGA analysis gives the same prediction as does the DGA analysis, and is consistent with the NDD analysis and the experimental observations.

Table 5. Nucleation of $\{10\bar{1}2\}$ secondary twin variants in the $(11\bar{2}4)[22\bar{4}\bar{3}]$ primary twin.

NDD Analysis							
Secondary twin	b_t	b_i	b_r^m	$\|b_i\|^2$	x	$\|xb_t\|^2$	$\|b_r^m\|^2$
$(10\bar{1}2)[\bar{1}011]$ T_1^I	**$\lambda[\bar{1}011]$**	**b_3**	**$[\overline{0.07}\ \overline{0.33}\ 0.40\ \overline{0.26}]$**	**8.70**	**3**	**3.24**	**5.16**
$(01\bar{1}2)[0\bar{1}11]$ T_2^I	**$\lambda[0\bar{1}11]$**	**b_3**	**$[\overline{0.33}\ \overline{0.07}\ 0.40\ \overline{0.26}]$**	**8.70**	**3**	**3.24**	**5.16**

DGA and m-DGA Analysis			
Secondary twin	Group	D_{ST} in the crystal reference frame of the parent grain	D_{ST} in the twinning reference frame of the primary twin
$(10\bar{1}2)[\bar{1}011]$ T_1^I	**I**	$\begin{bmatrix} 0.052 & 0.0901 & 0.1135 \\ 0.0049 & 0.0084 & 0.0106 \\ -0.0277 & -0.048 & -0.0604 \end{bmatrix}$	$\begin{bmatrix} 0 & 0.0544 & -0.1516 \\ 0 & -0.0218 & 0.0607 \\ 0 & -0.0078 & 0.0218 \end{bmatrix}$
$(01\bar{1}2)[0\bar{1}11]$ T_2^I	**I**	$\begin{bmatrix} 0.0604 & 0 & 0.0659 \\ 0.0852 & 0 & 0.093 \\ -0.0554 & 0 & -0.0604 \end{bmatrix}$	$\begin{bmatrix} 0 & -0.0544 & -0.1516 \\ 0 & -0.0218 & -0.0607 \\ 0 & 0.0078 & 0.0218 \end{bmatrix}$
$(\bar{1}102)[1\bar{1}01]$ T_3^I	II	$\begin{bmatrix} 0.0338 & -0.008 & 0.0059 \\ 0.1625 & -0.0383 & 0.0283 \\ 0.0258 & -0.0061 & 0.0045 \end{bmatrix}$	$\begin{bmatrix} 0.0337 & -0.0497 & -0.0424 \\ 0.0591 & -0.0872 & -0.0745 \\ -0.0424 & 0.0626 & 0.0535 \end{bmatrix}$
$(\bar{1}012)[10\bar{1}1]$ T_4^I	III	$\begin{bmatrix} 0.0412 & 0.006 & -0.0183 \\ 0.0913 & 0.0134 & -0.0406 \\ 0.1229 & 0.0180 & -0.0546 \end{bmatrix}$	$\begin{bmatrix} -0.0128 & 0.0047 & 0.0030 \\ 0.0591 & -0.0218 & -0.0138 \\ -0.1486 & 0.0548 & 0.0346 \end{bmatrix}$
$(0\bar{1}12)[01\bar{1}1]$ T_5^I	III	$\begin{bmatrix} 0.0625 & 0.079 & -0.0443 \\ -0.0062 & -0.0079 & 0.0044 \\ 0.077 & 0.0974 & -0.0546 \end{bmatrix}$	$\begin{bmatrix} -0.0128 & -0.0047 & 0.0030 \\ -0.0591 & -0.0218 & 0.0138 \\ -0.1486 & -0.0548 & 0.0346 \end{bmatrix}$
$(1\bar{1}02)[\bar{1}101]$ T_6^I	II	$\begin{bmatrix} 0.0466 & 0.1551 & 0.0275 \\ -0.0154 & -0.0511 & -0.0091 \\ 0.0076 & 0.0253 & 0.0045 \end{bmatrix}$	$\begin{bmatrix} 0.0337 & 0.0497 & -0.0424 \\ -0.0591 & -0.0872 & 0.0745 \\ -0.0424 & -0.0626 & 0.0535 \end{bmatrix}$

5. Discussion

For co-family double twins, only one double twin variant is selected in the preferred group of the double twins, which can be accurately predicted by using the m-DGA and NDD criteria. However, two double twin variants are possibly activated in the predominant group of the double twins belonging to non-family type, which fails to be distinguished by using the m-DGA and NDD criteria. The a-SF criterion is helpful for determining the competition between two double twin variants in the prevailed group of non-family double twins. In Fig. 4a, $C_2^I \rightarrow T_2^I$ is identified to be a $\{11\bar{2}2\}\rightarrow\{10\bar{1}2\}$ non-family double twin. In C_2^I primary twin, two secondary twins belong to predominant Group (Group II), i.e., T_4^I and T_5^I. According to the a-SF analysis, the loading direction identified for the grain in Fig. 4a, where C_2^I forms is located

at the predicted loading domain as shown in Fig. 10h, where the SF of T_2^I secondary twin variant is greater than T_3^I. In Fig. 4e, a detection of $C_4^I \rightarrow T_5^I$ double twin (Group II) is indicated. In C_4^I primary twin, both T_4^I and T_5^I belong to Group II. The a-SF analysis in Fig. 10i indicates that the loading direction identified for the grain is corresponding to a greater SF of T_5^I secondary twin variant than T_4^I.

As to $\{11\bar{2}4\}\rightarrow\{10\bar{1}2\}$ non-family double twins, the criteria based on m-DGA and NDD can fully account for the preference of Group I double twin variants. To determine the selection of two variants in Group I, the a-SF criterion is applied. In Fig. 5a, $C_6^{II} \rightarrow T_1^I$ double twin belonging to Group I is detected. In C_6^{II} primary twin, T_6^I and T_1^I are both Group I double twin variants. According to the a-SF analysis in Fig. 11h, the loading direction identified for the grain where C_6^{II} forms is located at the predicted loading domain, where the SF of T_6^I secondary twin variant is greater than T_1^I. In Fig. 5e, the detection of $C_4^{II} \rightarrow T_5^I$ double twin (Group I) is determined. In C_4^{II} primary twin, there are two secondary twins T_4^I and T_5^I belonging to Group I. The a-SF analysis in Fig. 11i indicates that the loading direction identified for the grain where C_4^{II} forms is located at the loading domain, where the SF of T_5^I secondary twin variant is greater than T_4^I.

Regarding the selection criteria, the a-SF clearly shows that the SFs for six twin variants are positive in most of the primary loading domain as long as the primary twin is subjected to a positive resolved shear stress, although it cannot predict the preferred secondary twin variants. The DGA focusing on the maximum relaxation of the strain created by the primary twins in the vicinity of the primary twin is not effective to predict the preferred secondary twin variant, while the m-DGA with the focus on minimizing the resultant plastic deformation due to the double twinning successfully predicts the preferred secondary twin variant. The success of the m-DGA prediction implies that the formation of double twin may be related to the minimization of the local shear associated with the primary twin in the matrix. Both m-DGA and NDD predict results agree with the experimental observations. These two theories speculate that nucleation of a secondary twin requires nucleation sources at the primary twin boundary and the accumulation and reaction of gliding dislocations at the primary twin boundary provide such nucleation sources. Such speculations reflect in general the physics of twinning.

6. Conclusions

Four types of double twins observed in deformed Ti specimens are classified into two families according to their zone axes: co-family double twins and non-family double twins. The co-family double twins include $\{11\bar{2}2\}\rightarrow\{11\bar{2}1\}$ ($C_i^I \rightarrow T_j^{II}$) and $\{11\bar{2}1\} \rightarrow \{11\bar{2}4\}$ ($T_i^{II} \rightarrow C_j^{II}$), where both twins share the zone axis $<10\bar{1}0>$. The non-family double twins include $\{11\bar{2}2\}\rightarrow\{10\bar{1}2\}$ ($C_i^I \rightarrow T_j^I$) and $\{11\bar{2}4\} \rightarrow \{10\bar{1}2\}$ ($C_i^{II} \rightarrow T_j^I$) that have different zone axes, one along $<11\bar{2}0>$ and the other along $<10\bar{1}0>$. Secondary twin variant selection is examined according to the apparent Schmid factor (a-SF) analysis, the displacement gradient accommodation (DGA) and the modified DGA (m-DGA) analysis, and the nucleation via dislocation dissociation (NDD). The theories were assessed by comparing the predictions with the experimental observations.

Co-family double twins can be categorized into four groups. For $\{11\bar{2}2\}\rightarrow\{11\bar{2}1\}$ double twins, the dominant double twins are described as $C_i^I \rightarrow T_i^{II}$. For $\{11\bar{2}1\} \rightarrow \{11\bar{2}4\}$ double twins, the dominant double twins are described as $T_i^{II} \rightarrow C_i^{II}$. In each primary twin, only one secondary twin variant is prevailed over other secondary twin variants according to the NDD and m-DGA analysis. The a-SF and DGA analyses reveal the relative possibility among six variants but cannot predict the preferred one.

Non-family double twins can be divided into three groups. For $\{11\bar{2}2\}\rightarrow\{10\bar{1}2\}$ double twins, the preferred double twins can be described as $C_i^I \rightarrow T_i^I$ or T_{i+1}^I. For $\{11\bar{2}4\} \rightarrow \{10\bar{1}2\}$ double twins, the preferred double twins can be described as $C_i^{II} \rightarrow T_i^I$ or T_{i+1}^I. The selection between the two variants obeys the SF rule. More importantly, the NDD and m-DGA can properly predict the preference of secondary twin variants. The a-SF and DGA fail to predict correctly the preferred secondary twin variants.

A correct prediction based on m-DGA and NDD also implies that selection of secondary twin variant in a double twin is deterministic because two facts, both m-DGA and NDD are geometric models and the resolved shear stress associated with secondary twinning is positive. The current study can help develop micro- and macro- scale predictive models of the deformation behavior of hexagonal materials [38-40].

Acknowledgement

Xu, Gong and Wang acknowledge supports from the US National Science Foundation (NSF) (CMMI-1661686). Jiang thanks the NSF support (CMMI-1462885).

References

[1] O. Ozugwu, M. Wang. Titanium alloys and their machinability, J. Mater. Proc. Tech 68 (1997) 262-274.
[2] L. Jiang, J.J. Jonas, R. Mishra, A. Luo, A. Sachdev, S. Godet. Twinning and texture development in two Mg alloys subjected to loading along three different strain paths, Acta Mater. 55 (2007) 3899-3910.
[3] C. Cepeda-Jiménez, J. Molina-Aldareguia, M. Pérez-Prado. Origin of the twinning to slip transition with grain size refinement, with decreasing strain rate and with increasing temperature in magnesium, Acta Mater. 88 (2015) 232-244.
[4] J. Del Valle, F. Carreño, O.A. Ruano. Influence of texture and grain size on work hardening and ductility in magnesium-based alloys processed by ECAP and rolling, Acta Mater. 54 (2006) 4247-4259.
[5] S. Dong, Q. Yu, Y. Jiang, J. Dong, F. Wang, L. Jin, W. Ding. Characteristic cyclic plastic deformation in ZK60 magnesium alloy, Int J Plast. 91 (2017) 25-47.
[6] C. Gu, L. Tóth. Polycrystal modeling of tensile twinning in a Mg alloy during cyclic loading, Scr Mater. 67 (2012) 673-676.
[7] H. Wang, P. Wu, J. Wang. Modeling inelastic behavior of magnesium alloys during cyclic loading–unloading, Int J Plast. 47 (2013) 49-64.
[8] L. Wu, S. Agnew, D. Brown, G. Stoica, B. Clausen, A. Jain, D. Fielden, P. Liaw. Internal stress relaxation and load redistribution during the twinning–detwinning-dominated cyclic deformation of a wrought magnesium alloy, ZK60A, Acta Mater. 56 (2008) 3699-3707.
[9] G. Proust, C.N. Tomé, A. Jain, S.R. Agnew. Modeling the effect of twinning and detwinning during strain-path changes of magnesium alloy AZ31, Int J Plast. 25 (2009) 861-880.
[10] Z.-Z. Shi, Y. Zhang, F. Wagner, T. Richeton, P.-A. Juan, J.-S. Lecomte, L. Capolungo, S. Berbenni. Sequential double extension twinning in a magnesium alloy: Combined statistical and micromechanical analyses, Acta Mater. 96 (2015) 333-343.
[11] Y. Xin, M. Wang, Z. Zeng, M. Nie, Q. Liu. Strengthening and toughening of magnesium alloy by {10-12} extension twins, Scr Mater. 66 (2012) 25-28.
[12] S. Agnew, M. Yoo, C. Tome. Application of texture simulation to understanding mechanical behavior of Mg and solid solution alloys containing Li or Y, Acta Mater. 49 (2001) 4277-4289.
[13] T. Al-Samman, X. Li. Sheet texture modification in magnesium-based alloys by selective rare earth alloying, Mater Sci Eng A. 528 (2011) 3809-3822.
[14] C. Cepeda-Jiménez, J. Molina-Aldareguia, M. Pérez-Prado. Effect of grain size on slip activity in pure magnesium polycrystals, Acta Mater. 84 (2015) 443-456.
[15] J.T. Wang, J.Q. Liu, J. Tao, Y.L. Su, X. Zhao. Effect of grain size on mechanical property of Mg–3Al–1Zn alloy, Scr Mater. 59 (2008) 63-66.
[16] J.R. Greer, J.T.M. De Hosson. Plasticity in small-sized metallic systems: Intrinsic versus extrinsic size effect, Prog Mater Sci. 56 (2011) 654-724.
[17] P. Partridge. The crystallography and deformation modes of hexagonal close-packed metals, Metall Rev. 12 (1967) 169-194.
[18] M. Yoo. Slip, twinning, and fracture in hexagonal close-packed metals, Metallurgical Transactions A 12 (1981) 409-418.
[19] A.A. Salem, S.R. Kalidindi, R.D. Doherty. Strain hardening of titanium: role of deformation twinning, Acta Mater. 51 (2003) 4225-4237.
[20] S. Xu, C. Schuman, J.-S. Lecomte. Accommodative twins at high angle grain boundaries in rolled pure titanium, Scr Mater. 116 (2016) 152-156.
[21] S. Xu, M. Gong, X. Xie, Y. Liu, C. Schuman, J.-S. Lecomte, J. Wang. Crystallographic characters of {11-22} twin-twin junctions in titanium, Philos Mag Lett. (2017) 1-13.
[22] L. Capolungo, I. Beyerlein. Nucleation and stability of twins in hcp metals, Phys Rev B. 78 (2008) 024117.
[23] S. Jin, K. Marthinsen, Y. Li. Formation of {11-21} twin boundaries in titanium by kinking mechanism through accumulative dislocation slip, Acta Mater. 120 (2016) 403-414.
[24] N.J. Lane, S.I. Simak, A.S. Mikhaylushkin, I.A. Abrikosov, L. Hultman, M.W. Barsoum. First-principles study of dislocations in hcp metals through the investigation of the (11-21) twin boundary, Phys Rev B. 84 (2011) 184101.
[25] L. Wang, R. Barabash, T. Bieler, W. Liu, P. Eisenlohr. Study of {11-21} Twinning in α-Ti by EBSD and Laue Microdiffraction, Metall Mater Trans A. 44 (2013) 3664-3674.
[26] S.J. Lainé, K.M. Knowles. {11-24} deformation twinning in commercial purity titanium at room temperature, Philos Mag. 95 (2015) 2153-2166.
[27] S. Wang, Y. Zhang, C. Schuman, J.-S. Lecomte, X. Zhao, L. Zuo, M.-J. Philippe, C. Esling. Study of twinning/detwinning behaviors of Ti by interrupted in situ tensile tests, Acta Mater. 82 (2015) 424-436.
[28] F. Xu, X. Zhang, H. Ni, Q. Liu. {11-24} deformation twinning in pure Ti during dynamic plastic deformation, Mater Sci Eng A. 541 (2012) 190-195.
[29] S. Xu, M. Gong, C. Schuman, J.-S. Lecomte, X. Xie, J. Wang. Sequential {10-12} twinning stimulated by other twins in titanium, Acta Mater. 132 (2017) 57-68.

[30] P. Zhou, D. Xiao, C. Jiang, G. Sang, D. Zou. Twin Interactions in Pure Ti Under High Strain Rate Compression, Metall Mater Trans A. 48 (2017) 126-138.
[31] W. Tirry, M. Nixon, O. Cazacu, F. Coghe, L. Rabet. The importance of secondary and ternary twinning in compressed Ti, Scr Mater. 64 (2011) 840-843.
[32] Q. Yu, Y. Jiang, J. Wang. Tension-compression-tension tertiary twins in coarse-grained polycrystalline pure magnesium at room temperature, Philos Mag Lett. 95 (2015) 194-201.
[33] I. Beyerlein, J. Wang, M. Barnett, C. Tomé. Double twinning mechanisms in magnesium alloys via dissociation of lattice dislocations. Proc. R. Soc. A, vol. 468: The Royal Society, 2012. p.1496-1520.
[34] J.J. Jonas, S. Mu, T. Al-Samman, G. Gottstein, L. Jiang, Ė. Martin. The role of strain accommodation during the variant selection of primary twins in magnesium, Acta Mater. 59 (2011) 2046-2056.
[35] É. Martin, L. Capolungo, L. Jiang, J.J. Jonas. Variant selection during secondary twinning in Mg–3% Al, Acta Mater. 58 (2010) 3970-3983.
[36] Y. Pei, A. Godfrey, J. Jiang, Y. Zhang, W. Liu, Q. Liu. Extension twin variant selection during uniaxial compression of a magnesium alloy, Mater Sci Eng A. 550 (2012) 138-145.
[37] Z.-Z. Shi, Y. Zhang, F. Wagner, P.-A. Juan, S. Berbenni, L. Capolungo, J.-S. Lecomte, T. Richeton. On the selection of extension twin variants with low Schmid factors in a deformed Mg alloy, Acta Mater. 83 (2015) 17-28.
[38] H. Qiao, S. Agnew, P. Wu. Modeling twinning and detwinning behavior of Mg alloy ZK60A during monotonic and cyclic loading, Int J Plast. 65 (2015) 61-84.
[39] H. Qiao, X. Guo, S. Hong, P. Wu. Modeling of {10-12}-{10-12} secondary twinning in pre-compressed Mg alloy AZ31, Journal of Alloys and Compounds 725 (2017) 96-107.
[40] H. Wang, P. Wu, J. Wang, C. Tomé. A crystal plasticity model for hexagonal close packed (HCP) crystals including twinning and de-twinning mechanisms, Int J Plast. 49 (2013) 36-52.
[41] S. Godet, L. Jiang, A. Luo, J. Jonas. Use of Schmid factors to select extension twin variants in extruded magnesium alloy tubes, Scr Mater. 55 (2006) 1055-1058.
[42] C. Gu, L. Toth, M. Hoffman. Twinning effects in a polycrystalline magnesium alloy under cyclic deformation, Acta Mater. 62 (2014) 212-224.
[43] I. Beyerlein, R. McCabe, C. Tomé. Effect of microstructure on the nucleation of deformation twins in polycrystalline high-purity magnesium: a multi-scale modeling study, J Mech Phys Solids. 59 (2011) 988-1003.
[44] K.D. Molodov, T. Al-Samman, D.A. Molodov, G. Gottstein. On the role of anomalous twinning in the plasticity of magnesium, Acta Mater. 103 (2016) 711-723.
[45] C. Tomé, I. Beyerlein, J. Wang, R. McCabe. A multi-scale statistical study of twinning in magnesium, JOM 63 (2011) 19-23.
[46] I. Beyerlein, C. Tomé. A probabilistic twin nucleation model for HCP polycrystalline metals. Proceedings of the Royal Society of London A: Mathematical, Physical and Engineering Sciences: The Royal Society, 2010. p.rspa20090661.
[47] I. Beyerlein, L. Capolungo, P. Marshall, R. McCabe, C. Tomé. Statistical analyses of deformation twinning in magnesium, Philos Mag. 90 (2010) 2161-2190.
[48] L. Wang, P. Eisenlohr, Y. Yang, T. Bieler, M. Crimp. Nucleation of paired twins at grain boundaries in titanium, Scr Mater. 63 (2010) 827-830.
[49] R. Xin, C. Guo, Z. Xu, G. Liu, X. Huang, Q. Liu. Characteristics of long {10-12} twin bands in sheet rolling of a magnesium alloy, Scr Mater. 74 (2014) 96-99.
[50] A. Serra, D. Bacon, R. Pond. The crystallography and core structure of twinning dislocations in hcp metals, Acta Metallurgica 36 (1988) 3183-3203.
[51] A. Serra, R. Pond, D. Bacon. Computer simulation of the structure and mobility of twinning disclocations in HCP Metals, Acta Metall. 39 (1991) 1469-1480.
[52] J. Wang, I. Beyerlein, J. Hirth, C. Tomé. Twinning dislocations on {-1011} and {-1013} planes in hexagonal close-packed crystals, Acta Mater. 59 (2011) 3990-4001.
[53] J. Wang, I. Beyerlein, C. Tomé. An atomic and probabilistic perspective on twin nucleation in Mg, Scr Mater. 63 (2010) 741-746.
[54] J. Wang, J.P. Hirth, C.N. Tomé. (-1012) Twinning nucleation mechanisms in hexagonal-close-packed crystals, Acta Mater. 57 (2009) 5521-5530.
[55] H. Qin, J.J. Jonas. Variant selection during secondary and tertiary twinning in pure titanium, Acta Mater. 75 (2014) 198-211.
[56] L. Bao, Y. Zhang, C. Schuman, J.-S. Lecomte, M.-J. Philippe, X. Zhao, C. Esling. Multiple twinning in pure hexagonal close-packed titanium, J Appl Crystallogr. 46 (2013) 1397-1406.
[57] M. Arul Kumar, I.J. Beyerlein, R.J. McCabe, C.N. Tome. Grain neighbour effects on twin transmission in hexagonal close-packed materials, Nat Commun 7 (2016) 13826.

[58] J. Bohlen, M.R. Nürnberg, J.W. Senn, D. Letzig, S.R. Agnew. The texture and anisotropy of magnesium–zinc–rare earth alloy sheets, Acta Mater. 55 (2007) 2101-2112.
[59] T. Bieler, P. Eisenlohr, C. Zhang, H. Phukan, M. Crimp. Grain boundaries and interfaces in slip transfer, Current Opinion in Solid State and Materials Science 18 (2014) 212-226.
[60] L. Capolungo, I. Beyerlein, C. Tomé. Slip-assisted twin growth in hexagonal close-packed metals, Scr Mater. 60 (2009) 32-35.
[61] L. Wang, Y. Yang, P. Eisenlohr, T. Bieler, M. Crimp, D. Mason. Twin nucleation by slip transfer across grain boundaries in commercial purity titanium, Metall Mater Trans A. 41 (2010) 421-430.
[62] M. Barnett, Z. Keshavarz, A. Beer, X. Ma. Non-Schmid behaviour during secondary twinning in a polycrystalline magnesium alloy, Acta Mater. 56 (2008) 5-15.
[63] S. Xu, L.S. Toth, C. Schuman, J.-S. Lecomte, M.R. Barnett. Dislocation mediated variant selection for secondary twinning in compression of pure titanium, Acta Mater. 124 (2017) 59-70.
[64] S. Mu, J.J. Jonas, G. Gottstein. Variant selection of primary, secondary and tertiary twins in a deformed Mg alloy, Acta Mater. 60 (2012) 2043-2053.

Figure captions

Fig. 1. Main twinning systems in α-titanium: (a) $\{10\bar{1}1\}$ twinning plane in yellow, $\{10\bar{1}2\}$ twinning plane in light blue and $\{10\bar{1}3\}$ twinning plane in red (b) $\{11\bar{2}1\}$ twinning plane in blue, $\{11\bar{2}2\}$ twinning plane in green and $\{11\bar{2}4\}$ twinning plane in pink.

Fig. 2. (a) An EBSD pattern of $\{11\bar{2}2\}\rightarrow\{11\bar{2}1\}$ double twins with twin boundaries indicated by color lines based on the misorientation axis/angle between the twin and grain in (b). In (c), the black dots represent six $\{11\bar{2}2\}$ twin planes in the matrix and the blue stars indicate six $\{11\bar{2}2\}$ twin planes in the primary twin. In (d), the the blue stars represent six $\{11\bar{2}1\}$ twin planes in the primary twin and the red squares indicate six $\{11\bar{2}1\}$ twin planes in the secondary twin.

Fig. 3 (a) An EBSD pattern of $\{11\bar{2}1\}\rightarrow\{11\bar{2}4\}$ double twins with twin boundaries indicated by different color according to the misorientation axis/angle between the twin and grain in (b). In (c), the black dots represent six $\{11\bar{2}1\}$ twin planes in the matrix and the blue stars indicate six $\{11\bar{2}1\}$ twin planes in the primary twin. In (d), the the blue stars represent six $\{11\bar{2}4\}$ twin planes in the primary twin and the red squares indicate six $\{11\bar{2}4\}$ twin planes in the secondary twin.

Fig. 4. Examples of $\{11\bar{2}2\}\rightarrow\{10\bar{1}2\}$ double twins: (a) $C_2^I \rightarrow T_2^I$ double twins with twin boundaries indicated by color lines according to the misorientation axis/angle between the twin and grain in (b). (e) $C_4^I \rightarrow T_5^I$ double twins with indicating the twin boundaries by colorful lines according to the misorientation axis/angle between the twin and grain in (f).In (c) and (g), the black dots represent six $\{11\bar{2}2\}$ twin planes in the matrix and the blue stars indicate six $\{11\bar{2}2\}$ twin planes in the primary twin. In (d) and (h), the the blue stars represent six $\{10\bar{1}2\}$ twin planes in the primary twin and the red squares indicate six $\{10\bar{1}2\}$ twin planes in the secondary twin.

Fig. 5. Examples of $\{11\bar{2}4\}\rightarrow\{10\bar{1}2\}$ double twins: (a) $C_6^{II} \rightarrow T_6^I$ double twins with twin boundaries indicated by color lines according to the misorientation axis/angle between the twin and grain in (b). (e) $C_4^{II} \rightarrow T_5^I$ double twins with indicating the twin boundaries by colorful lines according to the misorientation axis/angle between the twin and grain in (f).In (c) and (g), the black dots represent six $\{11\bar{2}4\}$ twin planes in the matrix and the blue stars indicate six $\{11\bar{2}4\}$ twin planes in the primary twin. In (d) and (h), the the blue stars represent six $\{10\bar{1}2\}$ twin planes in the primary twin and the red squares indicate six $\{10\bar{1}2\}$ twin planes in the secondary twin.

Fig. 6. (a) Stress domain where the SF of a C_1^I primary twin variant is positive and the largest among six possibilities. Under this stress domain, the SF of: (b) T_1^{II}, (c) T_2^{II}, (d) T_3^{II}, (e) T_4^{II}, (f) T_5^{II}, (g) T_6^{II} secondary twin variants.

Fig. 7. Crystallography of four groups of $\{11\bar{2}2\} \rightarrow \{11\bar{2}1\}$ double twins: (a) Group I and Group III, (b) Group II, (c) Group IV. The blue plane denotes the primary twin C_i^I, and the red plane represents the secondary twin T_j^{II}. The green dashed lines are the intersection between the primary twin C_i^I and the secondary twin T_j^{II}. The yellow planes outline the common slip planes where the intersection lines of the primary and secondary twin planes lie. (d) Illustration of the common line among a basal plane, a T_1^{II} twinning plane, a T_4^{II} twinning plane and a primary twin plane along $[1\bar{1}00]$. (e) Schematic of reaction of a basal <***a***> dislocation at a primary twin boundary into a T_1^{II} or a T_4^{II} twin dislocation plus a residual dislocation. (f) Illustration of the common line between a prismatic plane, a T_2^{II} twinning plane, a T_6^{II} twinning plane and a primary twin plane along $[11\bar{2}\bar{3}]$. (g) Schematic of reaction of a prismatic <***a***> dislocation at a primary twin boundary into a T_2^{II} or a T_6^{II} twin dislocation plus a residual dislocation.

Fig. 8. (a) Stress domain where the SF of a T_1^{II} primary twin variant is positive and the largest among six possibilities. Under this stress domain, the SF of: (b) C_1^{II}, (c) C_2^{II}, (d) C_3^{II}, (e) C_4^{II}, (f) C_5^{II}, (g) C_6^{II} secondary twin variants.

Fig. 9. Crystallography of four groups of $\{11\bar{2}1\} \rightarrow \{11\bar{2}4\}$ double twins. The blue plane denotes the primary twin T_i^{II}, and the red plane represents the secondary twin C_j^{II}. The green dashed line indicates the intersection between the primary twin T_i^{II} and the secondary twin C_j^{II}. The yellow plane outline the common slip plane where the intersection line of the primary and secondary twin plane lies.

Fig. 10. (a) Stress domain where the SF of a C_1^I primary twin variant is positive and the largest among six possibilities. Under this stress domain, the SF of: (b) T_1^I, (c) T_2^I, (d) T_3^I, (e) T_4^I, (f) T_5^I and (g) T_6^I secondary twin variants. (h) The SFs for secondary twin T_2^I in primary twin C_2^I. The black star indicates the loading direction associated with the grain in Fig. 4a. (i) The SFs for secondary twin T_5^I in primary twin C_4^I. The black star indicates the loading direction associated with the grain in Fig. 4e.

Fig. 11 (a) Stress domain where the SF of a C_1^{II} primary twin variant is positive and the largest among six possibilities. Under this stress domain, the SF of: (b) T_1^I, (c) T_2^I, (d) T_3^I, (e) T_4^I, (f) T_5^I and (g) T_6^I secondary twin variants. (h) The SFs for secondary twin T_6^I in primary twin C_6^{II}. The black star indicates the loading direction associated with the grain in Fig. 5a. (i) The SFs for secondary twin T_5^I in primary twin C_4^{II}. The black star indicates the loading direction associated with the grain in Fig. 5e.

Fig. 12. Crystallography of four groups of $\{11\bar{2}4\} \rightarrow \{10\bar{1}2\}$ double twins. The blue plane denotes the primary twin C_1^{II}, and the red plane represents the secondary twin T_j^I. The green dashed line indicates the intersection between the primary twin C_1^{II} and the secondary twin T_j^I. The yellow plane outlines the common slip plane where the intersection line of the primary and secondary twin plane lies.

Table captions

Table 1. Geometric characteristics of the primary twin and secondary twins.

Table 2. Nucleation of $\{11\bar{2}1\}$ secondary twin variants in the $(11\bar{2}2)[11\bar{2}\bar{3}]$ primary twin.

Table 3. Nucleation of $\{11\bar{2}4\}$ secondary twin variants in the $(11\bar{2}1)[\bar{1}\bar{1}26]$ primary twin.

Table 4. Nucleation of $\{10\bar{1}2\}$ secondary twin variants in the $(11\bar{2}2)[11\bar{2}\bar{3}]$ primary twin.

Table 5. Nucleation of $\{10\bar{1}2\}$ secondary twin variants in the $(11\bar{2}4)[22\bar{4}\bar{3}]$ primary twin

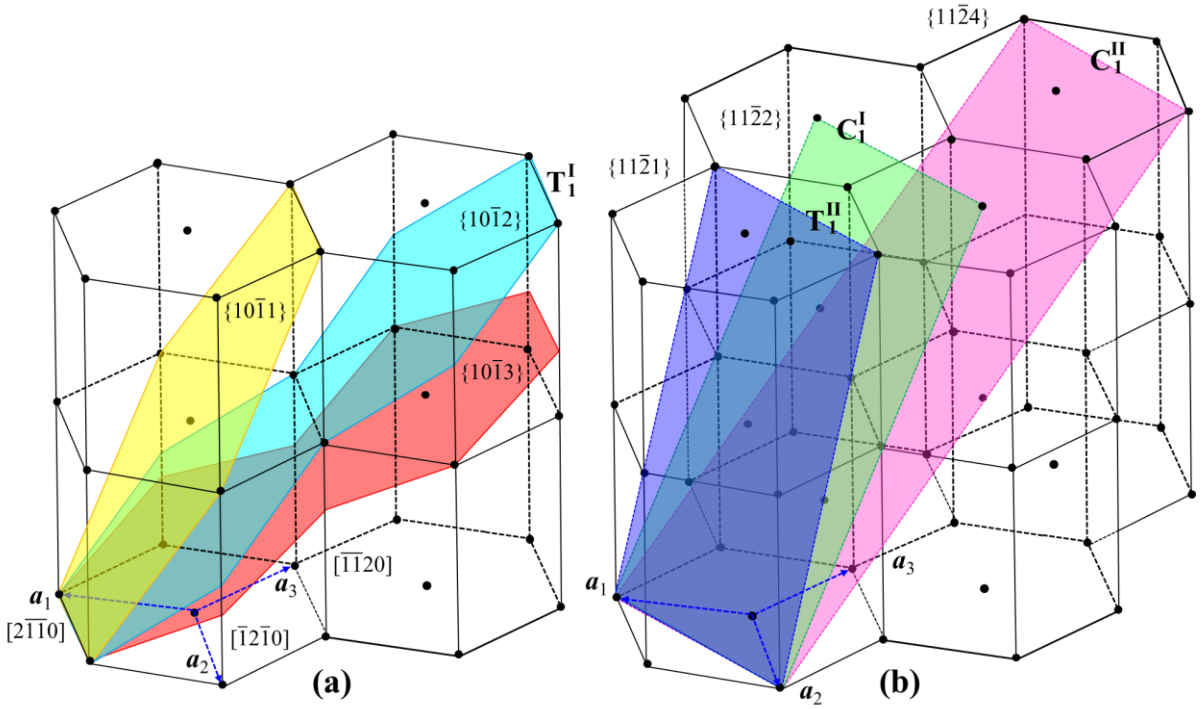

Fig. 1. Main twinning systems in α-titanium: (a) $\{10\bar{1}1\}$ twinning plane in yellow, $\{10\bar{1}2\}$ twinning plane in light blue and $\{10\bar{1}3\}$ twinning plane in red (b) $\{11\bar{2}1\}$ twinning plane in blue, $\{11\bar{2}2\}$ twinning plane in green and $\{11\bar{2}4\}$ twinning plane in pink.

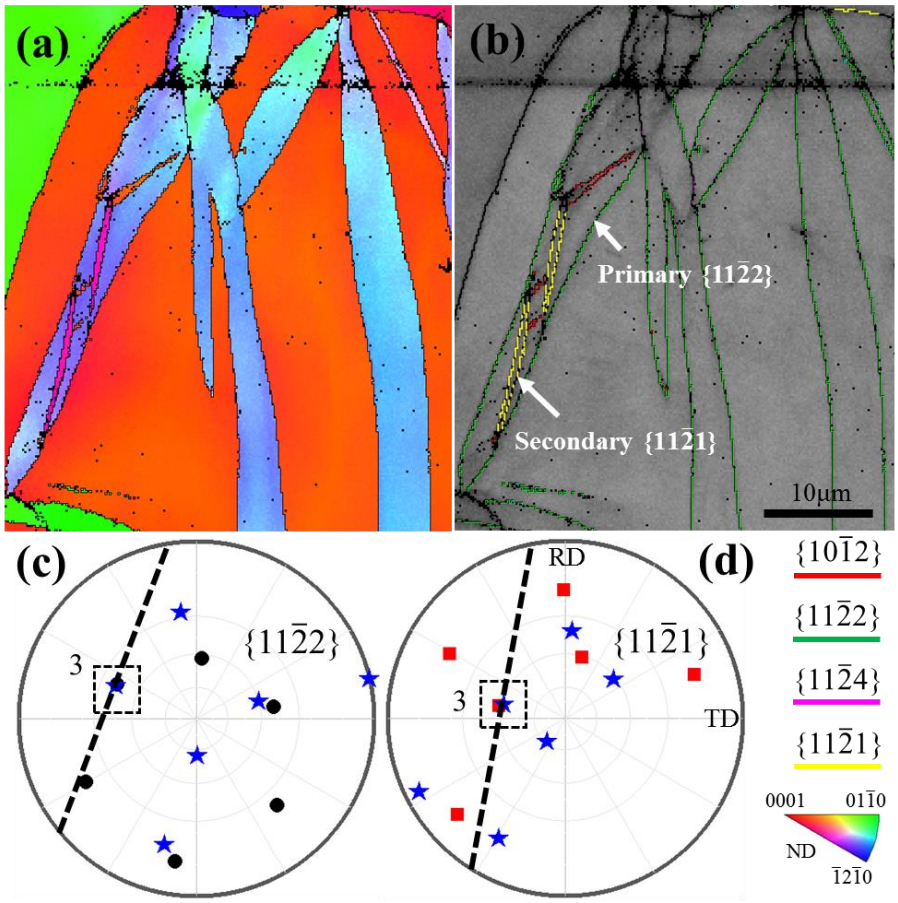

Fig. 2. (a) An EBSD pattern of {11$\bar{2}$2}→{11$\bar{2}$1} double twins with indicating the twin boundaries by colorful lines according to the misorientation axis/angle between the twin and grain in (b). In (c), the black dots represent six {11$\bar{2}$2} twin planes in the matrix and the blue stars indicate six {11$\bar{2}$2} twin planes in the primary twin. In (d), the the blue stars represent six {11$\bar{2}$1} twin planes in the primary twin and the red squares indicate six {11$\bar{2}$1} twin planes in the secondary twin.

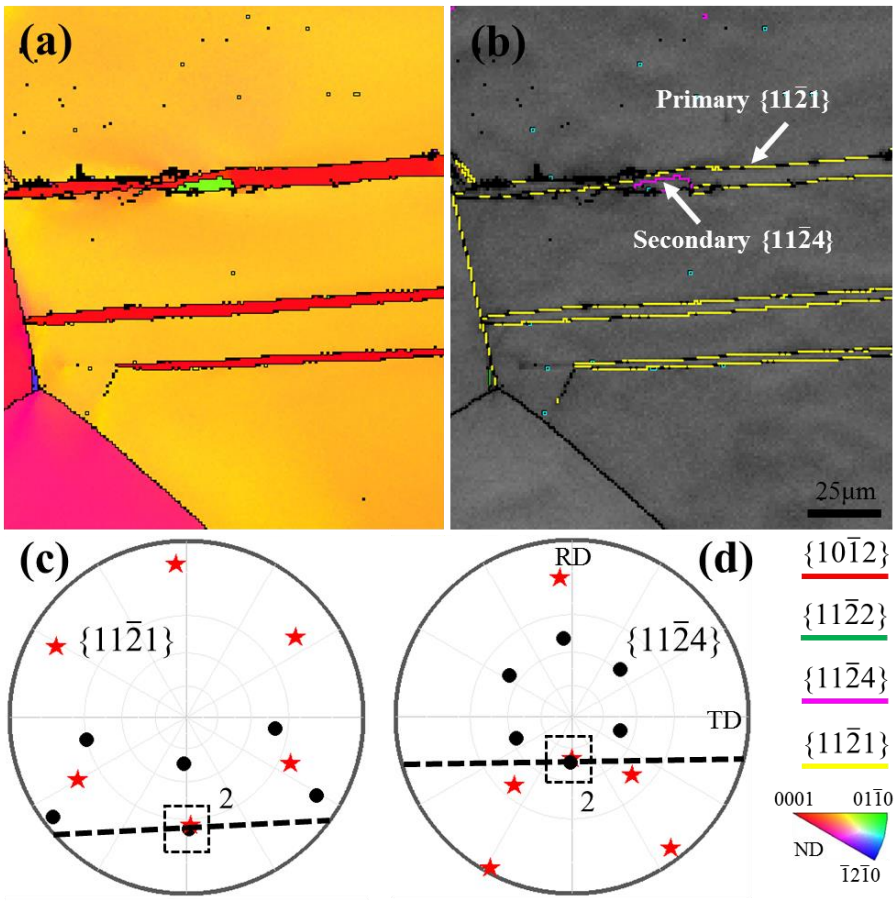

Fig. 3 (a) An EBSD pattern of {11$\bar{2}$1}→{11$\bar{2}$4} double twins with indicating the twin boundaries by colorful lines according to the misorientation axis/angle between the twin and grain in (b). In (c), the black dots represent six {11$\bar{2}$1} twin planes in the matrix and the blue stars indicate six {11$\bar{2}$1} twin planes in the primary twin. In (d), the the blue stars represent six {11$\bar{2}$4} twin planes in the primary twin and the red squares indicate six {11$\bar{2}$4} twin planes in the secondary twin.

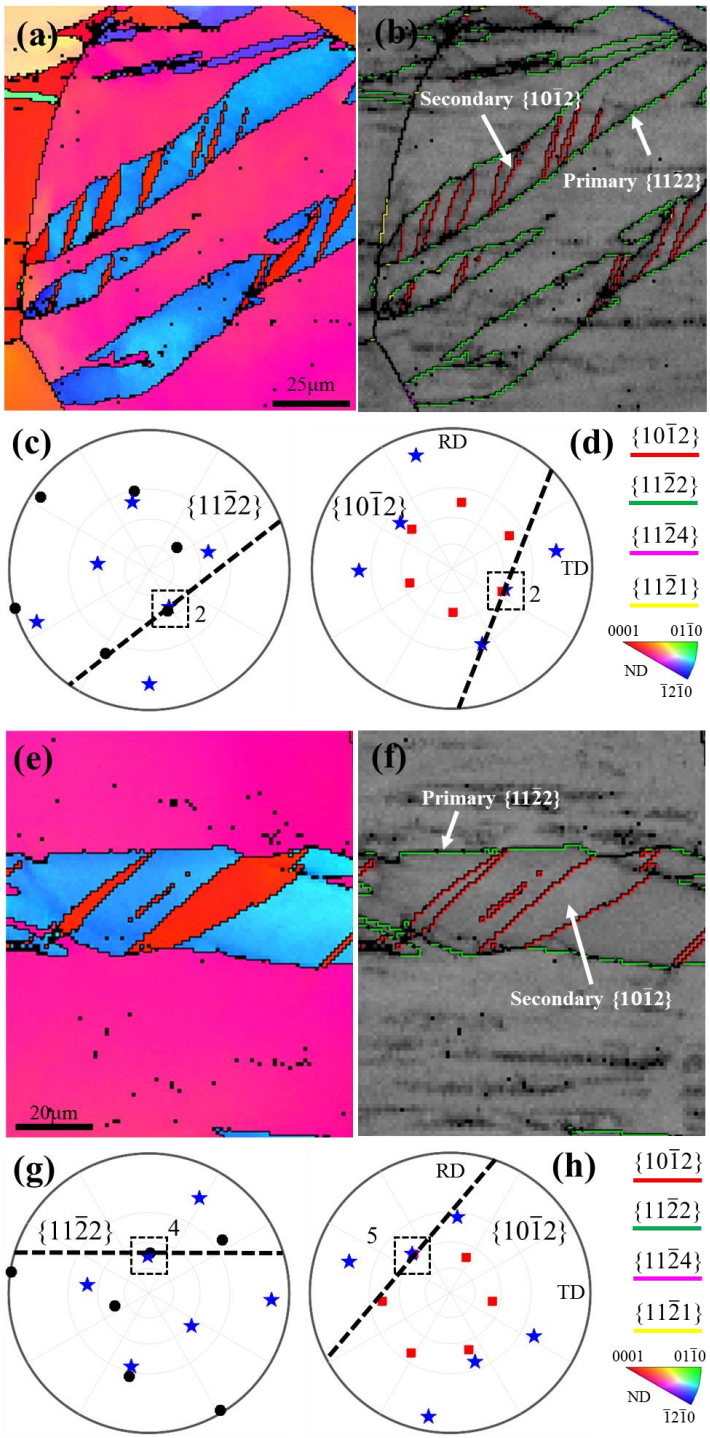

Fig. 4. Examples of $\{11\bar{2}2\}\rightarrow\{10\bar{1}2\}$ double twins: (a) $C_2^I \rightarrow T_2^I$ double twins with indicating the twin boundaries by colorful lines according to the misorientation axis/angle between the twin and grain in (b). (e) $C_4^I \rightarrow T_5^I$ double twins with indicating the twin boundaries by colorful lines according to the misorientation axis/angle between the twin and grain in (f).In (c) and (g), the black dots represent six $\{11\bar{2}2\}$ twin planes in the matrix and the blue stars indicate six $\{11\bar{2}2\}$ twin planes in the primary twin. In (d) and (h), the the blue stars represent six $\{10\bar{1}2\}$ twin planes in the primary twin and the red squares indicate six $\{10\bar{1}2\}$ twin planes in the secondary twin.

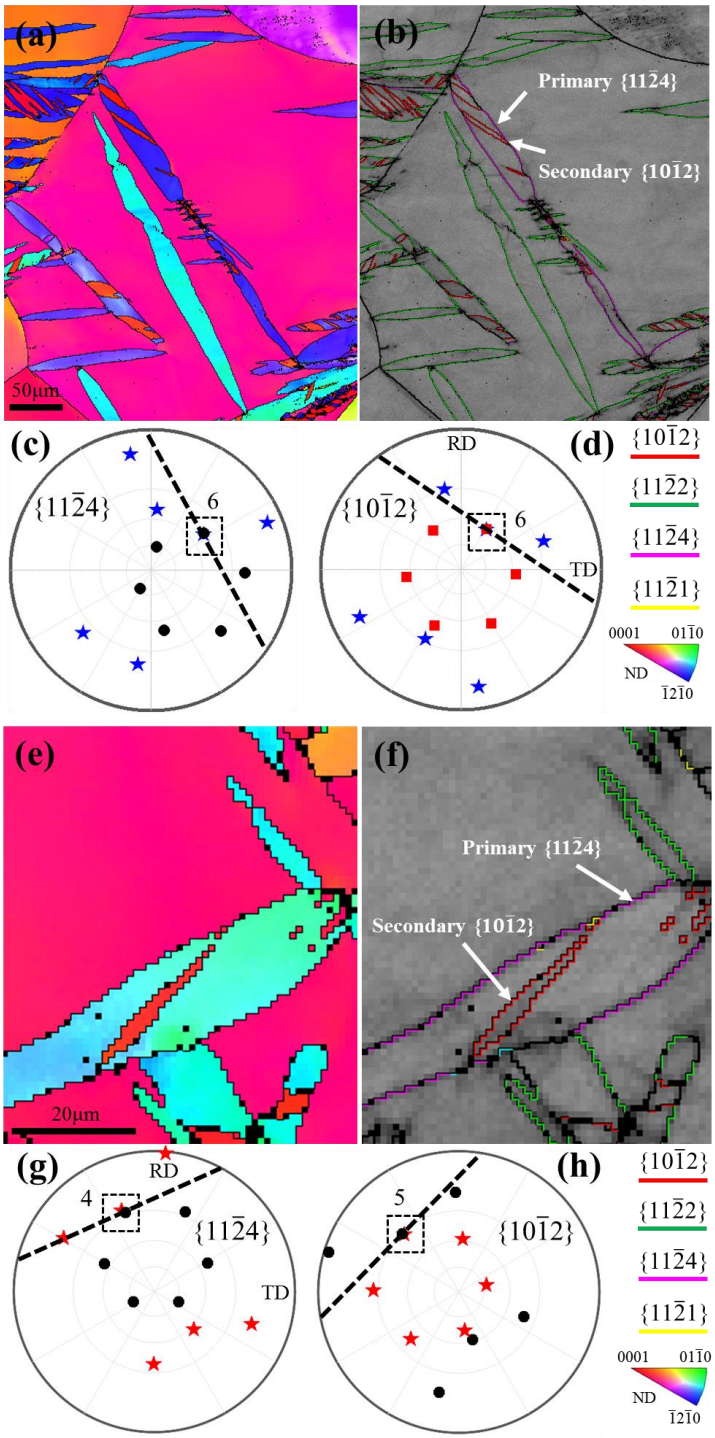

Fig. 5. Examples of {11$\bar{2}$4}→{10$\bar{1}$2} double twins: (a) $C_6^{II} \rightarrow T_6^I$ double twins with indicating the twin boundaries by colorful lines according to the misorientation axis/angle between the twin and grain in (b). (e) $C_4^{II} \rightarrow T_5^I$ double twins with indicating the twin boundaries by colorful lines according to the misorientation axis/angle between the twin and grain in (f).In (c) and (g), the black dots represent six {11$\bar{2}$4} twin planes in the matrix and the blue stars indicate six {11$\bar{2}$4} twin planes in the primary twin. In (d) and (h), the the blue stars represent six {10$\bar{1}$2} twin planes in the primary twin and the red squares indicate six {10$\bar{1}$2} twin planes in the secondary twin.

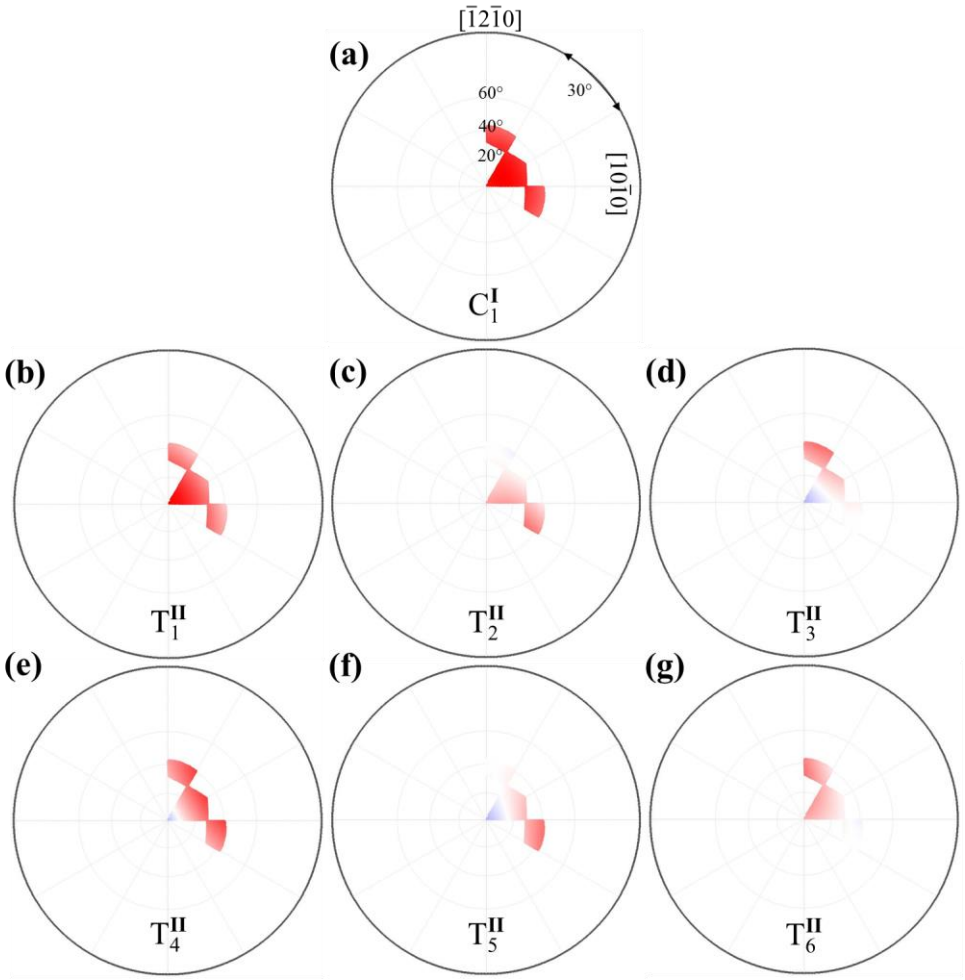

Fig. 6. (a) Stress domain where SF of C_1^I primary twin variant is positive and the largest among six possibilities. Under this stress domain, the SF of: (b) T_1^{II}, (c) T_2^{II}, (d) T_3^{II}, (e) T_4^{II}, (f) T_5^{II}, (g) T_6^{II} secondary twin variants.

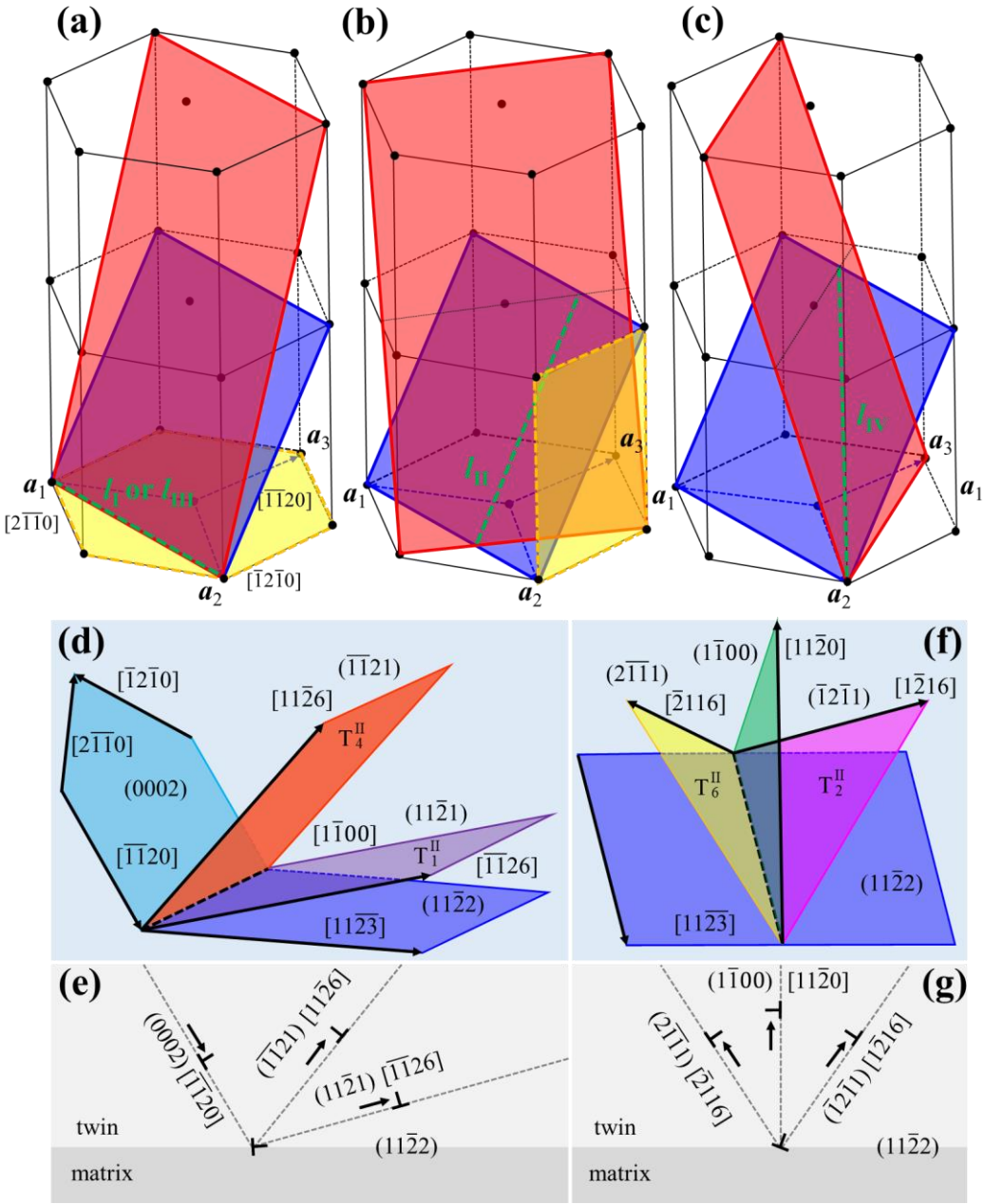

Fig. 7. Crystallography of four groups of $\{11\bar{2}2\} \rightarrow \{11\bar{2}1\}$ double twins: (a) Group I and Group III, (b) Group II, (c) Group IV. The blue plane denotes the primary twin C_i^{I}, and the red plane represents the secondary twin T_j^{II}. The green dashed line indicates the intersection between the primary twin C_i^{I} and the secondary twin T_j^{II}. The yellow plane outline the common slip plane where the intersection line of the primary and secondary twin plane lies. (d) Illustration of the common line between a basal plane, a T_1^{II} twinning plane, a T_4^{II} twinning plane and a primary twin plane along $[1\bar{1}00]$. (e) Schematic of reaction of a basal <*a*> dislocation at a primary twin boundary into a T_1^{II} or a T_4^{II} twin dislocation plus a residual dislocation. (f) Illustration of the common line between a prismatic plane, a T_2^{II} twinning plane, a T_6^{II} twinning plane and a primary twin plane along $[11\bar{2}3]$. (g) Schematic of reaction of a prismatic <***a***> dislocation at a primary twin boundary into a T_2^{II} or a T_6^{II} twin dislocation plus a residual dislocation.

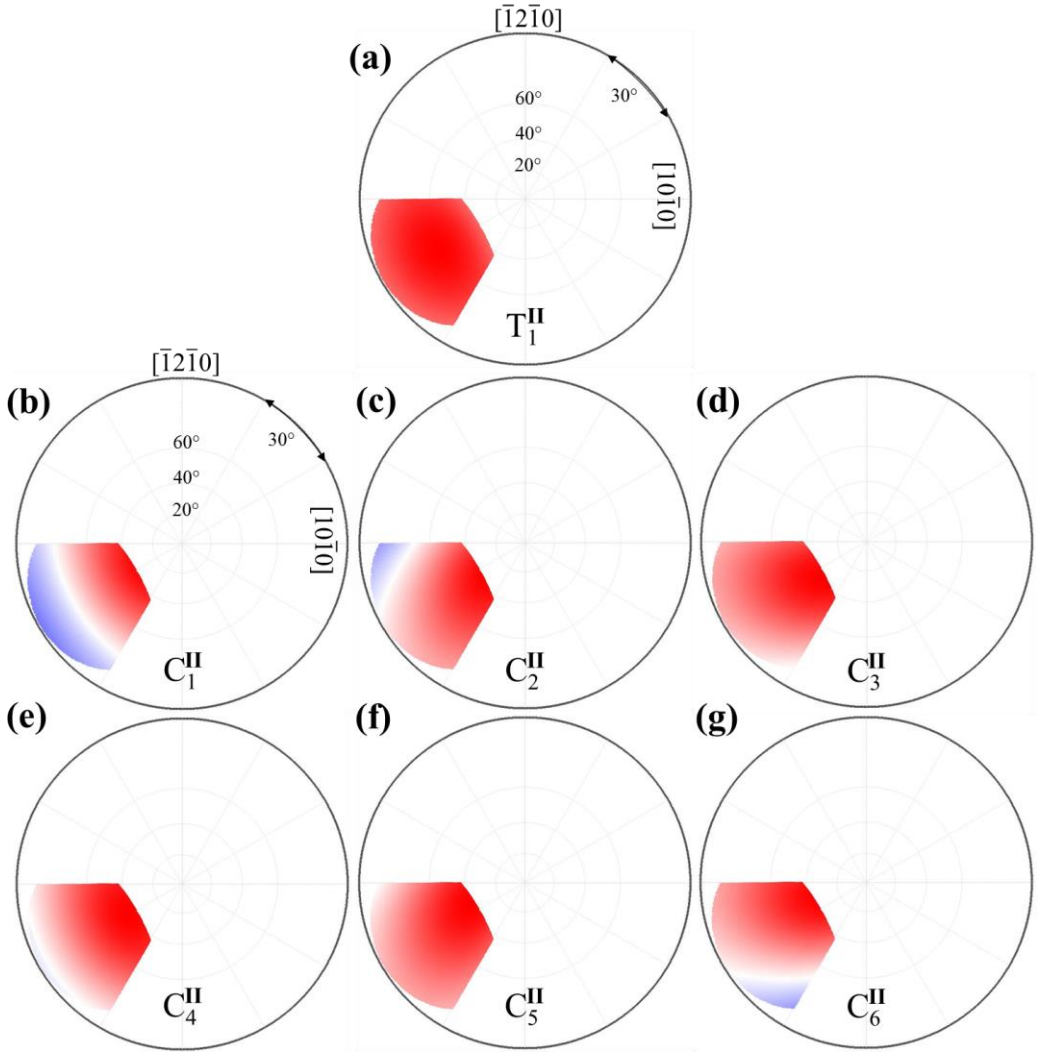

Fig. 8. (a) Stress domain where SF of T_1^{II} primary twin variant is positive and the largest among six possibilities. Under this stress domain, the SF of: (b) C_1^{II}, (c) C_2^{II}, (d) C_3^{II}, (e) C_4^{II}, (f) C_5^{II}, (g) C_6^{II} secondary twin variants.

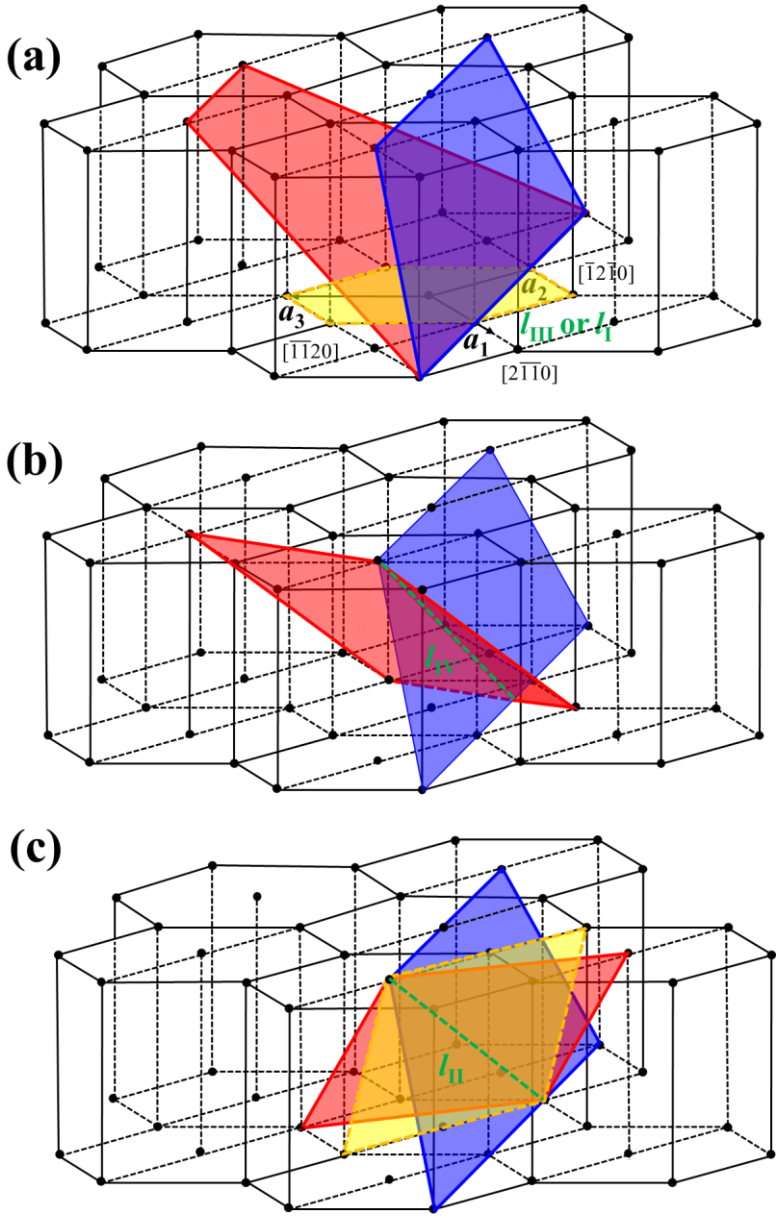

Fig. 9. Crystallography of four groups of $\{11\bar{2}1\} \rightarrow \{11\bar{2}4\}$ double twins. The blue plane denotes the primary twin T_i^{II}, and the red plane represents the secondary twin C_j^{II}. The green dashed line indicates the intersection between the primary twin T_i^{II} and the secondary twin C_j^{II}. The yellow plane outline the common slip plane where the intersection line of the primary and secondary twin plane lies.

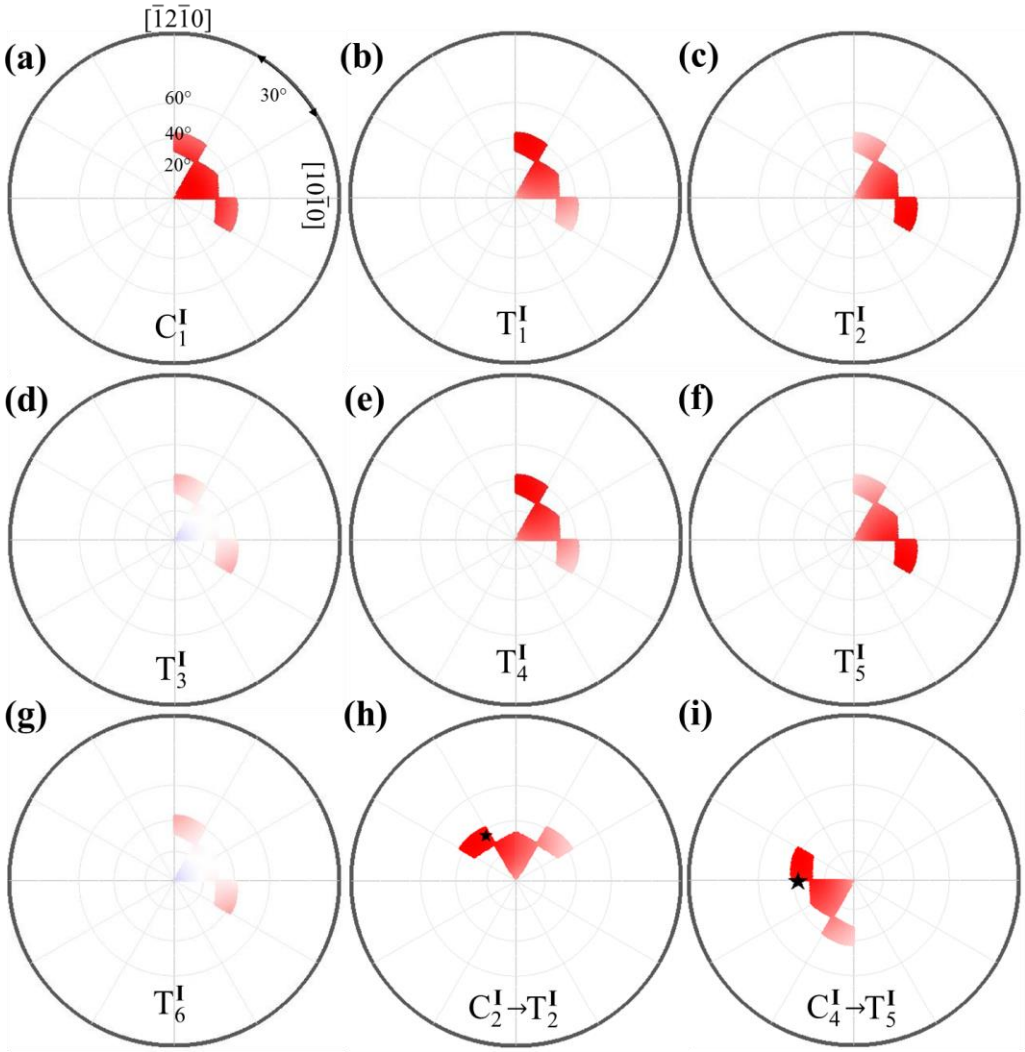

Fig. 10. (a) Stress domain where SF of C_1^I primary twin variant is positive and the largest among six possibilities. Under this stress domain, the SF of: (b) T_1^I, (c) T_2^I, (d) T_3^I, (e) T_4^I, (f) T_5^I and (g) T_6^I secondary twin variants. (h) The SFs for secondary twin T_2^I in primary twin C_2^I. The black star indicates the loading direction associated with the grain in Fig. 4a. (i) The SFs for secondary twin T_5^I in primary twin C_4^I. The black star indicates the loading direction associated with the grain in Fig. 4e.

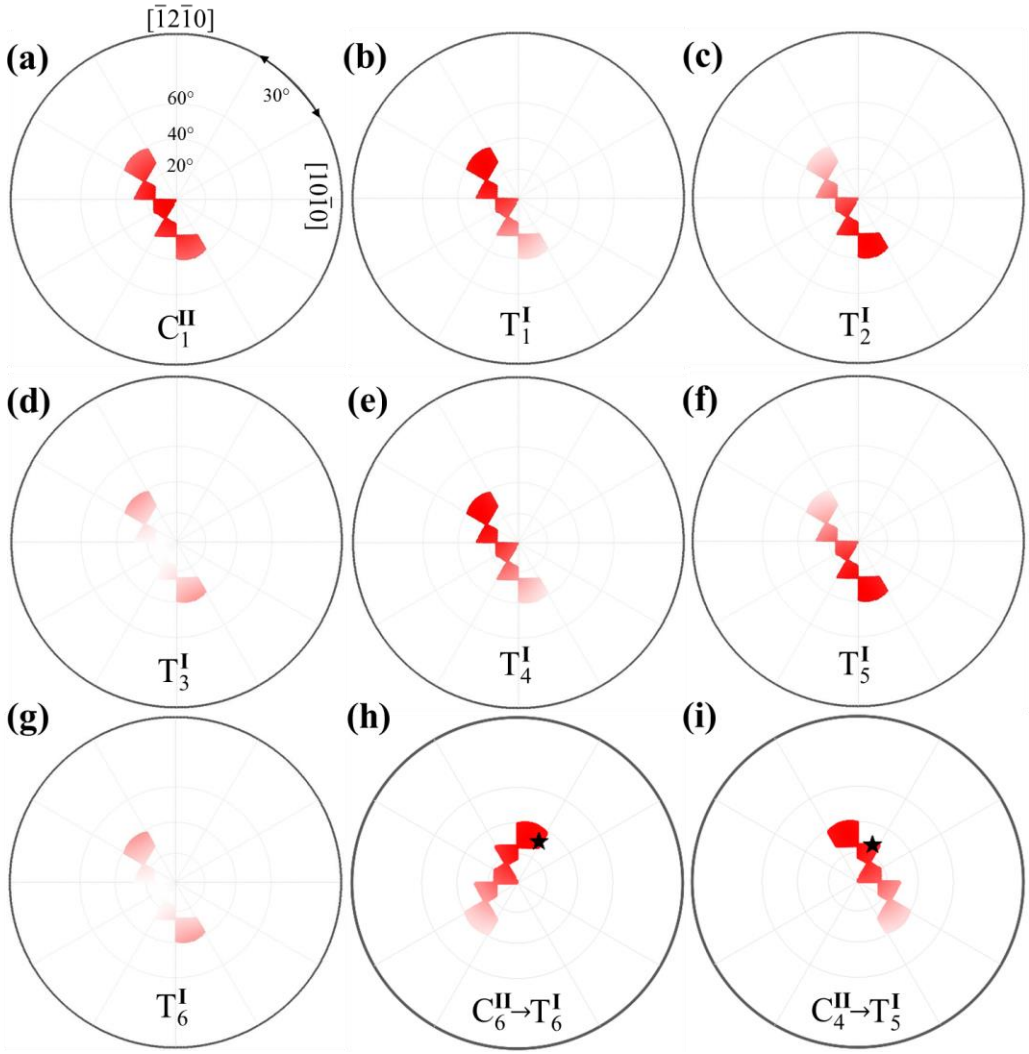

Fig. 11 (a) Stress domain where SF of C_1^{II} primary twin variant is positive and the largest among six possibilities. Under this stress domain, the SF of: (b) T_1^I, (c) T_2^I, (d) T_3^I, (e) T_4^I, (f) T_5^I and (g) T_6^I secondary twin variants. (h) The SFs for secondary twin T_6^I in primary twin C_6^{II}. The black star indicates the loading direction associated with the grain in Fig. 5a. (i) The SFs for secondary twin T_5^I in primary twin C_4^{II}. The black star indicates the loading direction associated with the grain in Fig. 5e.

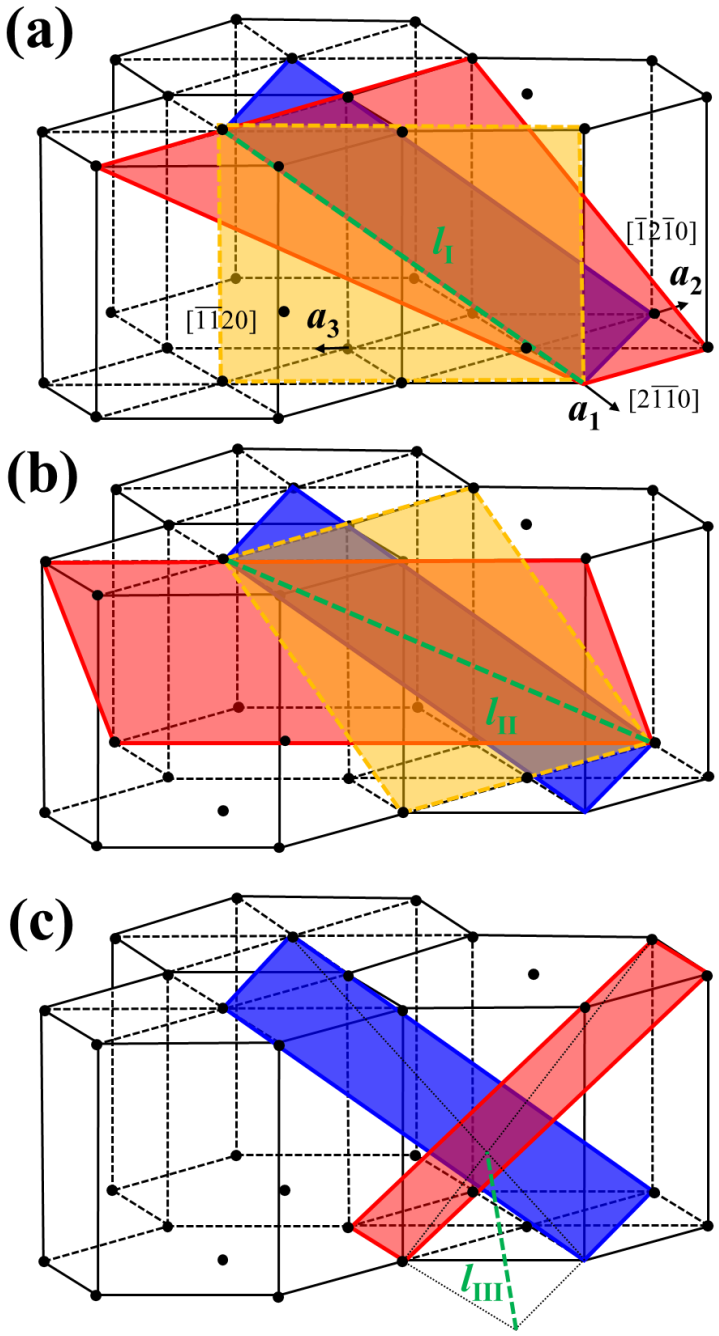

Fig. 12. Crystallography of four groups of $\{11\bar{2}4\} \rightarrow \{10\bar{1}2\}$ double twins. The blue plane denotes the primary twin C_l^{II}, and the red plane represents the secondary twin T_j^I. The green dashed line indicates the intersection between the primary twin C_l^{II} and the secondary twin T_j^I. The yellow plane outlines the common slip plane where the intersection line of the primary and secondary twin plane lies.